# Wave Scattering in Random Layered Media

by

**Jongchul Park**

A dissertation submitted to the Graduate Faculty in Physics in partial fulfillment of the requirements for the degree of Doctor of Philosophy, The City University of New York

2010

This manuscript has been read and accepted for the
Graduate Faculty in Physics in satisfaction of the
dissertation requirement for the degree of Doctor of Philosophy.

Professor Azriel Z. Genack

Date | Chair of Examining Committee

Professor Steven G. Greenbaum

Date | Executive Officer

Professor Vinod M. Menon

Professor Jerome Klosner

Professor Ying-Chin Chen

Professor Godfrey Gumbs

Supervisory Committee

THE CITY UNIVERSITY OF NEW YORK

Abstract

Wave Scattering in Random Layered Media

by

Jongchul Park

Advisor: Professor Azriel Z. Genack

The scaling and statistics of the transport of waves in random media depend strongly on the dimensionality of the medium. The statistic of transmission in one dimension (1D) and quasi-1D (Q1D) have been calculated and tested. However, the statistic for other dimensions has not been established. Exploring transport in a layered system of stacks of glass cover slips with transverse nonuniformity has allowed us to study a dimensional crossover in transport from 1D towards 3D. The crossover occurs when the lateral spread of the wave become larger than the transverse coherence length in the transmitted speckle pattern as the number of layers increases.

In thin samples, in which light does not spread beyond a single coherence area of the field on the output surface, the statistics of normalized intensity follow 1D statistics associated with a segment of a log-normal distribution with a sharp drop below the log-normal distribution for low values of intensity. Once the lateral spread is larger than the transverse coherence length, the probability density of intensity

becomes a mixture of a mesoscopic distribution and an intensity distribution of a Gaussian field. This distribution was originally found for Q1D. Beyond 1D, the intensity statistics have a same form as Q1D statistics which is a function of a single localization parameter, the "statistical conductance" $g'$. This transition from 1D to Q1D statistics reflects a topological change in the transmitted field. In 1D, the transmitted intensity never vanishes, while beyond 1D, a speckle pattern built upon a network of phase singularities forms.

Acknowledgments

First of all, I would like to thank my advisor, Professor Azriel Z. Genack for his encouragement and advice throughout my research work. I also would like to thank Drs. Vinod M. Menon, Godfrey Gumbs, Ying-Chin Chen and Jerome Klosner for being my supervisory committee.

My work could not been done without the help of Dr. Sheng Zhang from Chrial Photonics Inc. and Professor Valery Milner from the University of British Columbia, the 1D simulation program provided by Dr. Victor Kopp and valuable discussions with Jing Wang and Zhou Shi. I thank all these friends and also Samuel Gillman who helped with the experiment.

Finally, I would like to thank my family, my father who endlessly supports and believes in me, my mother who will happily congratulate me in heaven and my brother and sisters who always give support when I need it.

Again, thank all of you.

Table of Contents

List of Figures

# Chapter 1

# Introduction

## 1.1 General Introduction

Wave transport through a variety of complex media, such as clouds, fog, white paint, human tissue, electronic and optical devices, and metamaterials has been studied for decades and provides an understanding of the nature of wave propagation in complex media. The study of wave transport in random [1-5] and periodic [6-9] media has been stimulated by the analogies [10] with electron localization [11-13], universal conductance fluctuations [14-18] and forbidden band gap in semiconductors and insulators. We are especially interested in finding the common characteristics of waves transmitted through random layered media and providing a framework for the statistics of wave transport in three dimensional systems.

We consider multiply scattered waves with a wide distribution of path lengths as they propagate in a random medium. The probability that the wave arrives at a certain point within the medium is the square of the absolute value of the complex amplitudes of all waves reaching that point, $P = \left| a_1 e^{i\varphi_1} + a_2 e^{i\varphi_2} + \cdots \right|^2$, where $a_i$ and $\varphi_i$ are amplitudes and phases of waves. That probability is made up a sum of self product terms, $a_n^2$, and a sum of cross product terms, $a_n a_m e^{i(\varphi_n - \varphi_m)}$, which are

interference terms with other waves. Waves propagating in a random medium are normally so randomized that the amplitudes and phases of the waves are uniformly distributed. As a result, the average of the cross product terms vanishes, and the average of intensity involves only self product terms. The average over a random ensemble of the spatial and temporal intensity can then be described by the diffusion equation [4, 40, 61],

$$\frac{\partial I(r,t)}{\partial t} - D\nabla^2 I(r,t) + \frac{1}{\tau_a} I(r,t) = Q(r,t), \tag{1-1}$$

where $I(r,t)$ is intensity, $\tau_a$ is the absorption time, $D = v\ell / d$ is the diffusion coefficient, $v$ is the transport velocity, $\ell$ is the transport mean free path, $d$ is the dimensionality and $Q(r,t)$ is a source function.

The averaging out of the cross product terms in average transport is not always valid. Consider waves traveling from a certain point. A part of the waves will return to the original point along a random path by scatterings. There is also a possibility of traveling along the same random path traversed in opposite direction. Two such waves will interfere constructively at the original point and the cross product terms of the two paths will not be averaged out. Since the amplitude and phase associated with these partial waves are identical, the probability of return to the original point is proportional to $P = \left|\Psi_1 + \Psi_2\right|^2 = \left|ae^{i\varphi} + ae^{i\varphi}\right|^2 = 4a^2$, which is twice the return probability obtained for the incoherent sum,

$|\Psi_1|^2 + |\Psi_2|^2 = |ae^{i\varphi}|^2 + |ae^{i\varphi}|^2 = 2a^2$, where $\Psi_1$ and $\Psi_2$ are complex amplitudes for waves traveling along the two random paths.

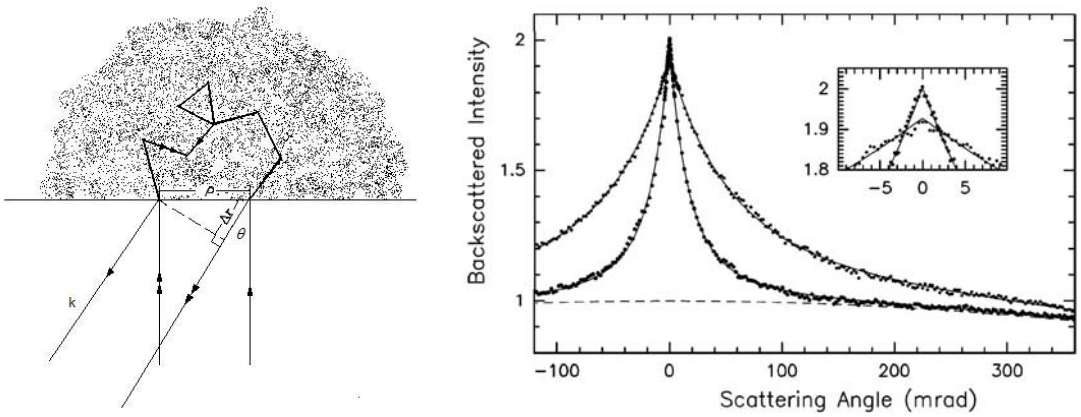


(a) (b)

Fig. 1-1 (a) Schematic of coherent backscattering from a random slab for a single pair of paths propagating along a path in opposite senses and (b) Coherence backscattering of light measured from a random slab with two different values for the transport mean free path $\ell$

We say that the wave is in the weak scattering limit when the probability of waves which return to a coherence volume, $V_c \sim (\lambda/2)^d$, where $\lambda$ is wavelength and $d$ is the dimensionality, is small [3]. Then the average of wave propagation over a random ensemble can well be described by the diffusion equation. As the scattering becomes stronger, constructive interference between the trajectories with closed loops becomes stronger and the probability of return to a coherence volume increases. This

is known as weak localization and leads to the enhancement of the backscattered intensity with respect to the classical prediction. The constructive interference between time-reversed paths of waves from a random slab leads to a sharp peak centered at the backscattering direction called coherent backscattering illustrated in Fig. 1-1 [19-24]. In the strong scattering limit, the return probability is enhanced and the constructive interference between the trajectories with closed loops is strong. This modifies average transport and eventually leads to the breakdown of diffusion and to Anderson localization [1]. Then wave propagation can no longer be described by the diffusion equation and the wave is localized. The energy of a localized wave has a maximum inside a random medium and decays approximately exponentially away from the peak, while the energy of a diffusive wave decays as $1/L^d$ from a source, where $L$ is sample length and $d$ is the dimensionality.

## 1.2 Anderson Localization

In 1958, Anderson proposed that electrons can be trapped in a small region of space by the constructive interference in strongly disordered three dimensional systems. The diffusion coefficient tends towards zero and conductance vanishes. Electrons are localized [11-13, 16, 25].

At room temperature, the typical inelastic scattering length of an electron in a system is around 10 nm because of thermal activation of atoms. The wave looses

temporal coherence and the constructive interference is washed out. The classical transport theory will well describe the flow of energy in the system. If the electronic system is cooled down to ≤ 1K, the inelastic collisions will be largely frozen out and the inelastic scattering length will reach the scale of several microns which is comparable to the electronic system in samples intermediate in size between the microscopic atomic scale and the macroscopic scale. In such mesoscopic systems, the wave is temporally coherent over the entire sample, though the wave rapidly looses spatial coherence. The classical transport theory which leads to Ohm's law fails and interference leads to enhanced fluctuation of the conductance because the conductance does not self-average.

In electrical systems with dimension, $d \leq 2$, the averaged conductance can be lowered by increasing size of the systems or strength of scattering, and electron transport is reduced. Beyond a critical size or strength of scattering, the diffusive motion of electrons is not simply reduced, it can be completely halted.

Studying photon localization makes it possible to observe pure Anderson localization because photons do not mutually interact. In addition, phase coherence is not lost at room temperature. The electromagnetic field and intensity and total transmission can be measured in both the near- and far-field in steady state and pulsed experiments. Suppressed transmittance, large non-Gaussian fluctuations of the intensity, nonexponential decay of pulsed transmission, and long-range correlations in the intensity are expected [40, 74, 76, 82].

The spatial distribution of intensity in samples and scaling of intensity for localized and diffusive waves are different. For 1D diffusive waves, the magnitude of the intensity inside a sample decreases linearly from a planar source and transmission falls inversely with sample thickness. For a localized wave, the magnitude of the wave on resonance with a localized state peaks inside the system and decays exponentially away from the peak [26]. An example of the exponential decay of a localized wave is illustrated in Fig. 1-2.

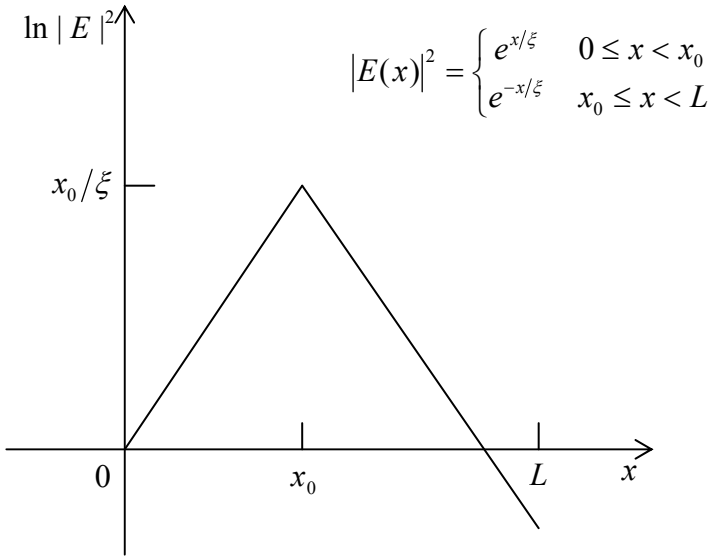


Fig. 1-2 Magnitude of a localized wave inside a random medium. $L$ is the sample length, $x_0$ is the position of the maximum in intensity, and $\xi$ is the localization length.

Transmission of localized waves peaks on resonance and the ensemble average of transmission decays exponentially beyond a length, $\overline{\xi}$,

$$\langle T(L) \rangle \sim \exp(-L/2\overline{\xi}), \tag{1-2}$$

where, $\overline{\xi}$ is the average exponential decay length or localization length, $L$ is the thickness of the sample and <...> represents the average over an ensemble of random sample configurations.

Localization in a random 1D [27], quasi-1D (Q1D) [28-32], 2D [33, 34], and 3D [35] system has been observed. In samples below the marginal dimension of 2, the probability of waves to return to a coherence volume can be controlled. As the sample size increases, the return probability increases. That is known as weak localization and leads to the enhancement of the backscattering intensity. Once the return probability exceeds unity, waves are localized. We see below why the marginal dimension is 2.

According to the solution of the diffusion equation, the probability density for a wave propagating in an unbounded random sample at distance $r$ from the origin at time $t$ is given by, $P(r,t) = (4\pi Dt)^{-d/2} \exp(-r^2/4\pi Dt)$, where $d$ is the spatial dimensionality and $D$ is the diffusion coefficient. The return probability to the origin is therefore given by [4]

$$\lim_{T\to\infty} \int_{2t_m}^{T} P(0,t)dt = \lim_{T\to\infty} \int_{2t_m}^{T} \frac{dt}{(4\pi Dt)^{d/2}}. \tag{1-3}$$

For $d$ = 1, 2 the integral diverges as $T \to \infty$, independent of $t_m$, which is the mean free time between scattering events. As a result, the wave is localized in sufficiently large one or two dimensional samples. For $d$ = 3, however, the return probability is proportional to $(8\pi D t_m)^{-1/2}$, so that the return probability may be less than unity. For $d$ = 3, when the Ioffe-Regel criterion, $k\ell \le 1$, is fulfilled [36], the return probability can be larger than unity since $t_m$ is small enough, here $\ell = \nu t_m$ is the transport mean free path and $\nu$ is the transport velocity. When $\ell \le 1/k = \lambda/2\pi$, the phase of the wave does not change much between scattering events, so the scattered waves strongly interfere with each other within a coherence volume and the waves can be localized.

Let us consider what kind of physical quantities indicate wave localization theoretically and experimentally and their behaviors in the diffusive and localization regimes. Some of the key indicators will be valid for nondissipative samples and some will be valid for only Q1D systems. One of the key indicators turns out to be valid even for 3D absorbing systems. The key indicators of localization are the Thouless number $\delta$ [13], the dimensionless conductance $g$, and the variance of ensemble averaged transmission coefficient $\mathrm{var}(s_{ab})$. The relationship between these parameters and the connection between mesoscopic fluctuations and localization are described below.

When we look at the transmission spectrum of a sample, we can see a series of peaks which correspond to the transmission modes of the sample. Denoting the average distance between neighboring modes as $\Delta\nu$, and the average linewidth of

modes as $\delta\nu$, we can define the Thouless number, $\delta$, as the ratio of the average of the linewidth of resonance modes and the average of spacing between the modes,

$$\delta = \frac{\delta\nu}{\Delta\nu}. \tag{1-4}$$

The average spacing between two neighboring modes varies inversely with the sample thickness, $\Delta\nu \sim 1/L^d$, where $L$ is sample length and $d$ is the dimensionality. $\Delta\nu$ is also inversely proportional to the Heisenberg time which is the longest time that a wave can travel inside a finite size sample without revisiting volumes within the sample. $\Delta\nu$ is also the inverse of the density of states of the sample, $\Delta\nu = 1/[n(\nu)AL]$, where $n(\nu)$ is the density of states per unit volume at frequency $\nu$ and $A$ is cross sectional area of the sample.

The scaling of the linewidth $\delta\nu$ is different for diffusive and localized waves. For diffusive waves, $\delta\nu$ is inversely proportional to the square of sample length, $\delta\nu \sim 1/L^2$, while for localized waves it decreases exponentially with sample length. If absorption can be neglected, $\delta\nu$, which is related to the leakage rate of energy from the sample, is inversely proportional to the average of the dwell time, the Thouless time, of waves inside the sample, $\delta\nu \sim 1/\delta t$. The enhancement of the integrated energy inside the sample corresponds to lengthened dwell time and narrowed linewidths of the resonances. With the presence of absorption within the sample the linewidth $\delta\nu$ will be broadened due to additional loss of energy and shortened dwell time, and the Thouless number $\delta$ will increase.

When the linewidth is larger than the level spacing, $\delta > 1$, the modes overlap spectrally and those spectrally overlapped modes may lead to modes overlapping in space. This leads a spatial distribution of the wave extending throughout the sample. Hence, $\delta > 1$ corresponds to diffusive waves. When $\delta < 1$, on the other hand, the modes are exponentially localized in different parts of the sample and are weakly coupled, and the transport is suppressed [38]. The Thouless number $\delta$ can serve as a key indicator of localization.

We will see another key parameter for localization, the dimensionless conductance *g*. In electronic systems, the dimensionless conductance *g*, is defined as $g = G/(e^2/h)$, where *G* is the conductance, *e* is the electron charge, and *h* is Planck's constant. More generally, *g* may be expressed via the Landauer relation in terms of the optical transmittance [39],

$$g = G/(e^2/h) = \left\langle \sum_{a,b} T_{ab} \right\rangle = \left\langle \sum_{a} T_a \right\rangle = \langle T \rangle, \tag{1-5}$$

where, $T_{ab}$ is the transmission coefficient for an incoming transverse mode *a* into the outgoing mode or a point on the output surface *b*, and $T_a$ is the total transmission which is the sum of $T_{ab}$ over all outgoing modes *b*, and *T* is the transmittance which is sum of $T_a$ over all incoming modes *a*. This is shown schematically in Fig. 1-3.

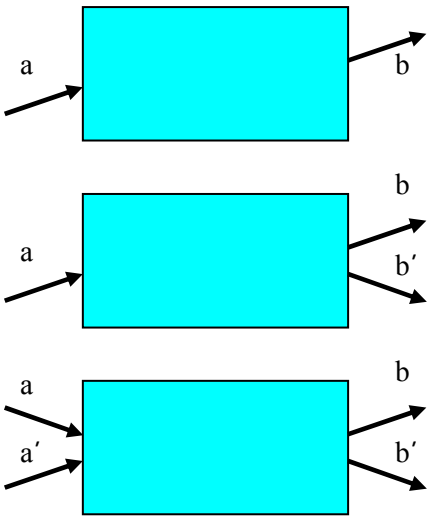


Fig. 1-3 Three key transmission quantities in multi-mode samples with increasing degrees of spatial averaging.

For electronic systems, the direct proportionality between the conductivity $\sigma$, and the diffusion coefficient $D$, is found from the "Einstein relation", $\sigma = (e^2/h)Dn(\nu)$ where $n(\nu)$ is the density of states per unit volume at frequency $\nu$. Combining the Einstein relation and Ohm's law $G = \sigma A/L$, $\delta\nu = D/L^2$, and $\Delta\nu = 1/[n(\nu)AL]$, the dimensionless conductance is shown to equal the Thouless number. Here $A$ is cross sectional area of the sample and $L$ is sample length,

$$g = G/(e^2/h) = Dn(\nu)\frac{A}{L} = \frac{D/L^2}{1/n(\nu)AL} = \frac{\delta\nu}{\Delta\nu} = \delta . \qquad (1\text{-}6)$$

Waves are localized when $g < 1$. $g$ is sensitive to the dimensionality and changes with sample length. For diffusive transport, $g \sim L^{d-2}$, while $g \sim \exp(-L/2\xi)$ for localized waves where $\xi$ is the average localization length. With the help of above relations, one may find the scaling function, $\beta(g) = d \ln g / d \ln L$, which describes how the dimensionless conductance *g* changes with system size *L*, depends only upon *g* itself and the dimensionality of the system, *d*.

The variance of the intensity and total transmission normalized by their ensemble averages, $s_{ab} = T_{ab} / < T_{ab} >$ and $s_a = T_a / < T_a >$, respectively, are also key markers for localization. In the absence of absorption, var($s_{ab}$) and var($s_a$) can be expressed in terms of the average value of the dimensionless conductance *g* in Q1D [28, 30, 40-42], var($s_{ab}$) $= 4/3g + 1$ and var($s_a$) $= 2/3g$. When absorption is present, the dimensionless conductance *g* decreases while the Thouless number $\delta$ increases, and neither of these is a reliable indicator of localization even though the localization length is not affected by absorption. However, var($s_{ab}$) and var($s_a$) are still reliable markers for localization in such systems. In a 3D slab system, the dimensionless conductance *g* and var($s_a$) cannot be defined because there is no specific area for the total transmission. The only remaining key maker is then var($s_{ab}$).

Here, we define a new parameter, $g'$, the "statistical conductance", in terms of the marker var($s_{ab}$),

$$g' = \frac{4}{3[\mathrm{var}(s_{ab}) - 1]}. \tag{1-7}$$

$g'$ scales inversely with sample thickness $L$ for $g' > 1$ and falls exponentially for $g' < 1$, as predicted for the localization parameter $g$. Waves are localized, when $g' < 1$. We will present our study of the statistics of normalized intensity transmitted through stacks of glass cover slips in Chapter 3.

The granular spatial variation of scattered intensity produced by the superposition of randomly scattered waves has been of wide interest since the invention of the laser in 1960. An example of a speckle pattern is shown in Fig. 1-4. The bright-dark intensity pattern is a fingerprint of a particular realization of the random sample. The speckle pattern is built upon a network of phase singularities at zeros of intensity. At these points, both the real and imaginary parts of the field are zero. Vortices of phase and current circulation centered on phase singularities have been observed. Equiphase lines emanate from phase singularities at points of vanishing intensity and show a $\pi$ radian jump at singularities between two equiphase lines opposite to each other. The statistical study of the motion of the phase singularities helps one to understand diffusive and localized waves in random samples. Field and intensity correlation functions can be obtained from measurements of the scattered field.

The intensity correlation function has a short-range term, which is the square of the absolute value of the field correlation function, and a long-range term. The

short-range term decays in the transverse length and gives the average size of speckle spots. In Q1D samples, a constant correlation is observed at large distances. This strong correlation leads to giant fluctuations in total transmission. var($s_{ab}$) can be obtained from an analysis of the intensity speckle pattern.

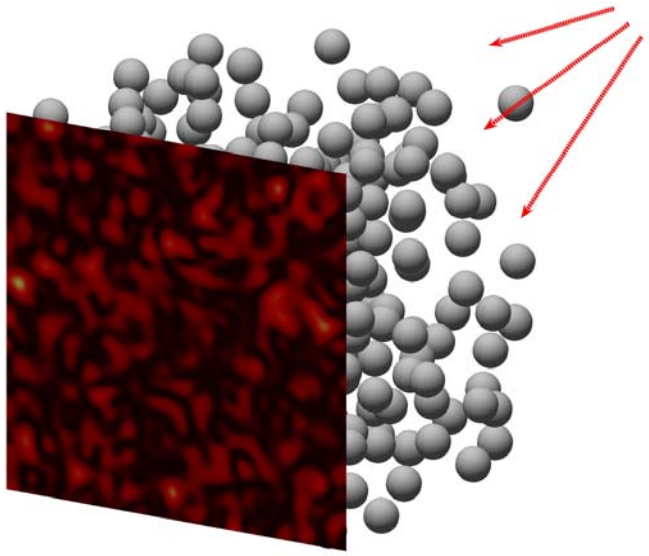

Fig. 1-4 Schematic of speckle pattern produced by multiple scattering in a random medium

## 1.3 Random Layered media

The study of wave propagation in layered structures which are found widely in nature, e.g. the earth′s crust, is of great interest. Here, we consider the propagation of a light beam normal to a stack of glass slides with nearly parallel surfaces. If the layers are perfectly parallel, then the propagation of an incident plane wave will be described as perfectly one-dimensional (1D). But, since perfectly parallel layered structures do not exist and some degree of transverse disorder is always present, the wave will be scattered off the line of incidence and will spread along the transverse direction with an increasing angular spread of the transmitted wave with increasing numbers of layers, $L$. Then, how we can say whether wave propagation is 1D? This can be answered by considering the lateral transverse spread of the wave, the transverse coherence length in the transmitted speckle pattern, and the angular distribution of the wave in the far-field [43]. These related characteristics of the wave influence the probability distribution of transmitted intensity in the near field. We find that propagation is 1D as long as the lateral transverse spread of the wave is smaller than the transverse coherence length. Propagation is transformed from 1D to 3D as the transverse spread of the wave increases. We have observed this transformation in studies of the scaling of total transmission and the changing of the statistics of normalized intensity as the number of layers increases.

Measurements of propagation were made with use of a linearly polarized helium-neon laser incident upon a stack of Corning cover slips as shown in Fig. 1-5.

The sample is composed of the glass cover slips with intervening air gaps. The cover slips are 22×22 $mm^2$ with average thickness of 150 μm. Each cover slip has a slight wedge with a standard deviation in the wedge angle between the front and back face of ~ $0.05^o$. The refractive index of the cover slip is 1.522 at the 632.8 nm wavelength, the helium-neon laser used in the experiment.

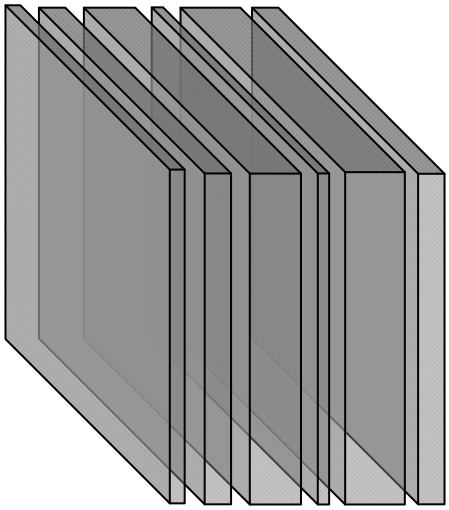

Fig. 1-5 Schematic of a random layered sample. The cover slips have an area of 22×22 $mm^2$ with average thickness of 150 μm and standard deviation of the wedge angle of ~ $0.05^o$. The refractive index of the cover slip is 1.522 at the 632.8 nm wavelength.

# Chapter 2

# Photon Delocalization Transition in Dimensional Crossover in Layered Media

## 2.1 Introduction

Layered media [44] are ubiquitous in geological, biological, electronic, and photonic settings. Understanding transport in these largely 1D structures embedded in three-dimensional space is of particular interest because of the critical role of dimensionality in wave propagation and localization.

When the number of times a partial wave winds its way through typical coherence volumes within the disordered sample exceeds unity, classical and quantum waves become exponentially peaked or localized [12, 13, 45, 46], otherwise the waves spread over the sample. The probability that a partial wave returns to a point is reinforced by the constructive interference of waves following time reversed paths and is facilitated in low-dimensional systems which restrict the volume explored by the wave. As a result, localization can always be achieved in sufficiently large 1D and 2D samples even when scattering is weak [13]. In 3D, however, localization can only be realized when scattering is sufficiently strong, so that the

mean free path $\ell$ is substantially smaller than the wavelength, which may be expressed as, $k\ell < 1$ [47], where $k = 2\pi/\lambda$ is the wave vector.

Examples of 1D localization have been observed for acoustic waves along a wire to which masses are randomly attached [48], microwave radiation in single-mode metallic waveguides with random dielectric inserts [49], and infrared radiation in single-mode fibers with random Bragg gratings [50]. A 1D description [51] is also suitable in the case of plane wave illumination of an unbounded medium comprised of parallel layers. It has been used to describe the localization of electrons in semiconductor superlattices [52] and photons in parallel dielectric layers of random thickness [53-55, 64].

Measurements of the scaling of average optical transmission, $< T(L) >$, for a normally incident beam in an ensemble of random stacks of overhead transparencies [54] and glass cover slips [55] were in accord with 1D simulations. Transmission approached the asymptotic limit, $< T(L) > \sim \exp(-L/2\xi)$, where $\xi$ is the localization length corresponding to the average exponential decay length of localized modes within the sample [54, 55]. Transmission in such samples is mediated by the excitation of states with single or multiple exponential peaks [46] in the spatial intensity distribution [45, 49, 56, 57]. Localized modes in layered samples play a particularly important role in amplifying media since such modes are long-lived because of their weak coupling to the boundaries. Low-threshold lasing was

demonstrated in a stack of glass cover slips and dye sheets when the pump laser and emission spectrum overlapped localized modes near the center of the sample [55].

Though propagation and lasing in layered media has been extensively investigated, the impact of nonuniformity within the layers upon transport has not been explored. Instead, studies of waves in random layered media have focused on their localization perpendicular to presumed uniform layers. In this chapter, we describe a crossover from localized towards diffusive propagation with increasing thickness and disorder in random layered media with nonparallel interfaces. Beyond the crossover point, transmission departs from the results of 1D simulations and approaches an inverse rather than an exponential falloff with sample thickness. This reflects a change in dimensionality of wave transport from 1D to 3D accompanied by a change from localized to diffusive propagation with increasing sample thickness.

The crossover occurs because destructive interference, which results in localization in samples with uniform layers of random thickness, is washed out as wave trajectories spread beyond a coherence length in the transmitted speckle pattern due to transverse disorder.

## 2.2 Transverse Nonuniformity of the Random Layered Samples

We studied transmission of a linearly polarized single frequency helium-neon laser at 632.8 nm through stacks of 22×22 $mm^2$ glass cover slips with refractive index $n$ = 1.522 and average thicknesses 150 μm. The glass stacks are held in place between two rings of 18-mm inner diameter. Since the thickness of the glass cover slips and of the air gap between them is not uniform, a normally incident beam is scattered from the normal direction to produce a speckled intensity pattern at the output. In single glass cover slips, the transmitted interference pattern gives the orientation and angle of the wedge between the surfaces of the cover slip.

The intensity at the output surface of the sample can be measured by imaging the output with a lens onto a CCD camera or by scanning one end of a single mode optical fiber over the output surface with the other end connected to a photodiode. Though, rapid measurements can be made with the CCD, the intensity of highly collimated light such as the light transmitted through a small number of cover slips, is modulated on a fine scale by interference in reflection from the CCD chip and the glass window in front of the CCD. Examples of maps of transmitted intensity obtained using the CCD for single cover slips are shown in Fig. 2-1.

Thinner fringes with uniform spacing are present in all images of Fig. 2-1 as a result of interference within the CCD assembly. This can be avoided by measuring the intensity with an optical fiber which is scanned over the output surface [see Fig. 2-2]. Measuring the spacing of the thicker fringes, $a$, yields the local wedge angle

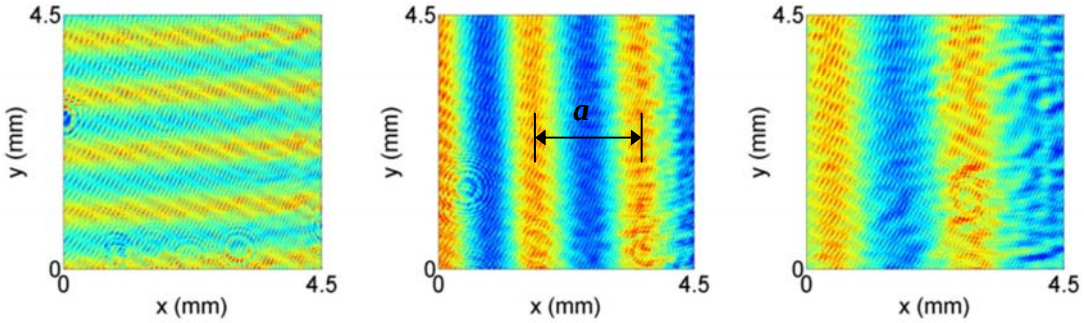


Fig. 2-1 Examples of CCD image of the fringe pattern for single cover slips

between the two faces of the cover slips, which is in a direction perpendicular to the fringes. The wedge angles of the cover slips are laid in plains nearly parallel to the sides of the cover slip. The measured fringe spacing $a$ in a group of 100 cover slips indicates a wedge angle with standard deviation of ~0.05 deg from the relation, $2na\theta \approx \lambda$, where $\lambda$ is wavelength of helium-neon laser and $n$ is the refractive index of the glass cover slips.

To measure the near-field image without instrumental interference fringes, we scanned a cleaved optical fiber over the sample. The end of the fiber was placed close to the sample output surface and translated in the plane with use of a micrometer motion stage. Examples of intensity pattern measured with the optical fiber with one and two cover slips are shown in Fig. 2-2. The air gaps between cover slips are nonuniform because of deviations from flatness of the glass surfaces as well as because of occasional dust particles. This is seen in intensity patterns generated by

two cover slips. With increasing $L$, the angular distribution of transmitted radiation grows so the scale of intensity variation in the transmitted speckle pattern shrinks. Intensity patterns in thick stacks of cover slips are shown in Chapter 3.

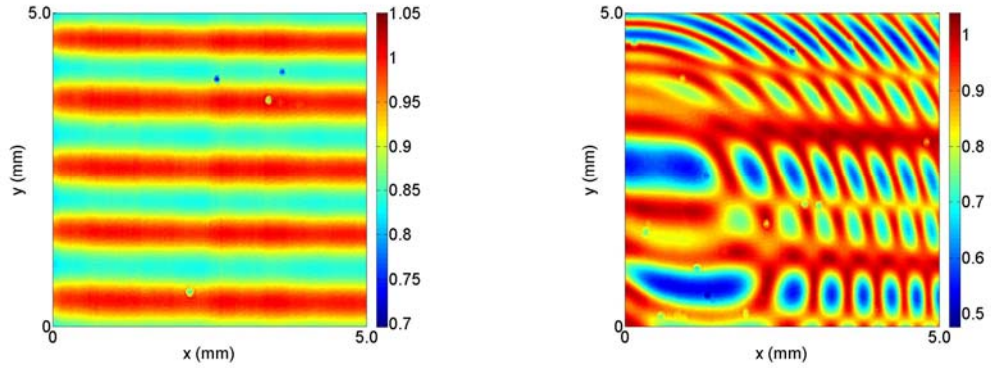


(a) (b)

Fig. 2-2 Examples of intensity pattern measured by the optical fiber (a) with single cover slip (b) with two cover slips. The local transmission coefficient indicated by the color bar may exceed unity due to the interference of waves with wave vector components in the layer plane.

## 2.3 Ensemble Average of Transmission

Wave propagation in 1D layered media can be modeled using the transfer or scattering matrix method. The main difference between these two methods is that the transfer matrix method relates electric fields in a layer to those in another layer while the scattering matrix method relates incoming to outgoing electric fields. The

scattering matrix method is numerically more stable than the transfer matrix method. We will discuss it further in Chapter 4.

The scattering matrix method was used for 1D simulations of over three million configurations of a given length. The refractive index was taken to be 1.522 for glass cover slips and 1 for air layers. The thickness of glass slides and averaged thickness was estimated to be in the ranges of 140-160 μm and 150 μm, respectively, from measurements form a group of 100 cover slips. By measuring the thickness of a stack of 100 cover slips, the average thickness of air layers was estimated to be 6 μm. The results of 1D simulations shown as black dots in Fig. 2-3 shows that $< T(L) >$ falls exponentially for large $L$ and are compared with measurements.

To measure the ensemble average of transmission in samples of $L$ slides, a collimated 500 μm single frequency helium-neon laser at 632.8 nm was projected normally on to the stack of the glass cover slips. The first surface of the stack was placed at the waist of the laser beam. To collect the transmission, an integrating sphere was placed immediately after the glass cover slips. Transmission was averaged by translating the sample over a 100 $mm^2$ area in 10 different stacks of cover slips. Different configurations were made by changing a part of or all of the slides to new slides and shuffling them. The measured ensemble average of transmission is plotted with red squares in Fig. 2-3 and compared with 1D simulations.

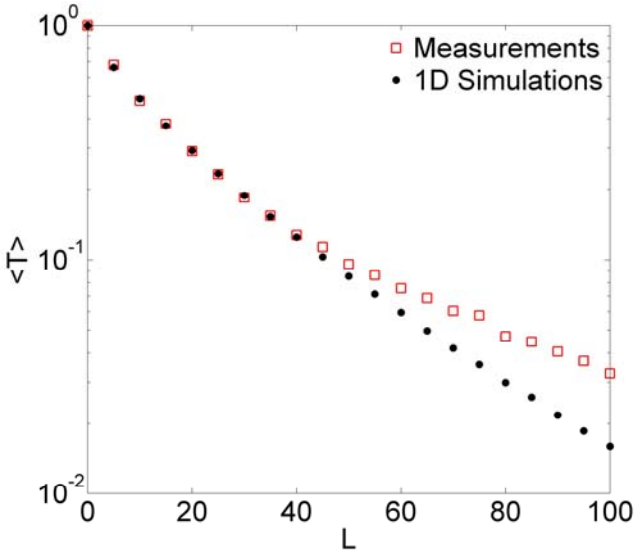


Fig. 2-3 Semilogarithmic plot of measurements (red squares) and 1D simulations (black dots) of $< T(L) >$.

As seen in Fig. 2-3 measurements of $< T(L) >$ are in agreement with 1D simulations up to $L$ = 40 but fall more slowly than 1D simulations for larger $L$. The departure of measurements of $< T(L) >$ from 1D simulations can be understood by comparing the superposition of corresponding rays in samples with parallel and nonparallel interfaces shown schematically in Figs. 2-4(a) and 2-4(b). The two wave trajectories $\alpha$ and $\beta$ in a sample with parallel interfaces shown in Fig. 2-4(a) pass through each cover slip the same number of times and are therefore of equal length. However, since light reflects from a higher index medium in one of the two additional

reflections in path $\beta$, the partial waves for the two paths are out of phase by $\pi$ rad and interfere destructively at the output surface of the sample. As the number of slides increases, the relative weight of such pairs of out of phase trajectories increases leading to an exponential falloff of $< T(L) >$ [54].

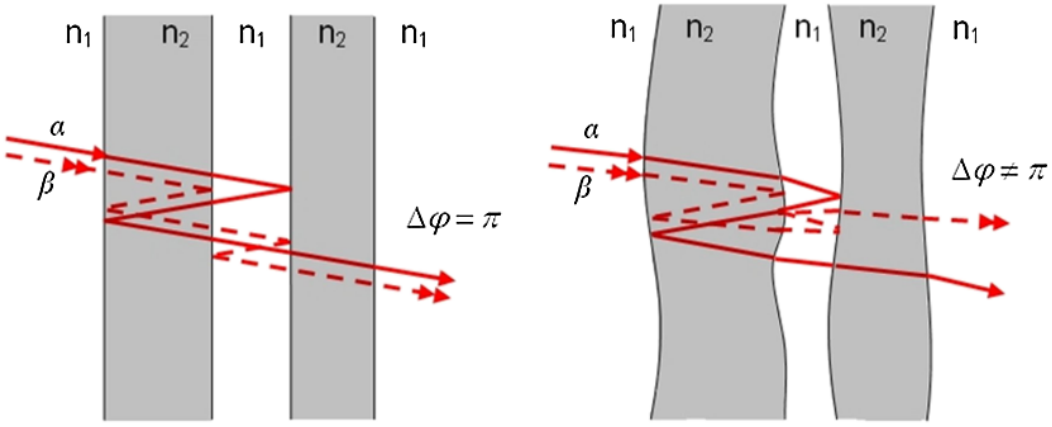


(a) (b)

Fig. 2-4 (a) and (b) Schematic of interference between partial waves following two trajectories, $\alpha$ and $\beta$, which pass through the same layers an equal number of times, in samples with parallel and nonparallel layers, respectively.

In a sample with nonparallel interfaces, the trajectories are distorted as shown schematically in Fig. 2-4(b). An additional phase difference between the two partial waves accumulates since trajectories cross the layer at different points at which the layer thicknesses differ and the angle between trajectories are no longer equal. As a result, the path lengths for the two trajectories differ. The phase difference between such pairs of trajectories is thereby increasingly randomized as the spatial and angular spread of the beam increases with increasing number of cover slips or local wedge angles. The reduced destructive interference of transmission of such paired trajectories leads to a slower decay of $< T(L) >$. In the limit in which the correlation between such pairs of partial waves vanishes, $< T(L) >$ falls as $1/L$ indicating that wave transport becomes diffusive [58].

The above considerations show that nonuniformity within the layers reduces the impact of localization on transmission. We expect therefore that when the nonparallism of the layers increases, $< T(L) >$ will depart from 1D simulations at smaller $L$. This is confirmed in measurements in samples created by inserting narrow metal shims at alternating edges of the glass cover slips as shown in Fig. 2-5. The red curve in Fig. 2-5 is the calculation for photon diffusion, naïve ray theory [54], utilizing the intensity reflection coefficient at the air-glass interface, $R = [(n-1)/(n+1)]^2$. The falloff of $< T(L) >$ approaches the diffusive limit as the wedge angle increases since the phases of trajectories are no longer correlated and the phase difference between different trajectories is randomized.

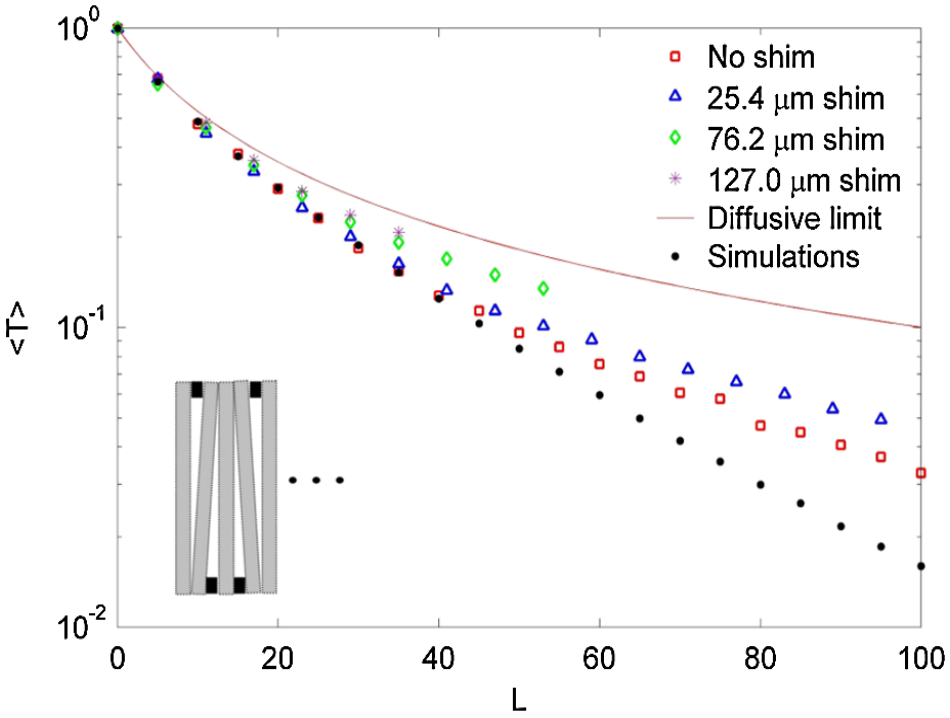


Fig. 2-5 Comparison of $< T(L) >$ for samples with different additional wedge angles. Thin shims with different thicknesses are inserted between layers to introduce average wedge angles of 0.073°, 0.218°, and 0.364°, respectively, into the air gaps. The side of the cover slip in which the shims are placed is alternated so that the average angle of the cover slips is not changed. The total transmission could only be measured up to thicknesses at which the beam spread does not approach the edges of the cover slips.

## 2.4 Dimensional Crossover of Wave Propagation

We saw that the ensemble average of transmission in layered systems initially follow 1D simulations and then depart from it as the number of slides increases. That is because nonuniformity within the layers reduces the impact of localization on transmission as the dimensionality increases since the chance of return to a coherence volume falls. An indication of the dimensionality of the system can be deduced by comparing the average transverse displacement between trajectories starting at the same input point and field coherence length at the output surface.

### 2.4.1 Measurement of Coherence Length

In a sample in which the field is Gaussian, the field correlation length can be readily obtained from the short-range component of the intensity correlation function. In the present case, however, the analysis of intensity correlation is complex because of strong localization effects and because the underlying disorder influences field statistics on the scale of the transverse spread of the wave. We therefore chose to obtain the field correlation function in the near field, $\Gamma(\Delta x, \Delta y) =< E(x, y)E^*(x + \Delta x, y + \Delta y) >$ , from measurements of the ensemble average of angular distribution of intensity in the far-filed, $< I(k_x, k_y) >$, known as the specific intensity. Since the far-field angular distribution of the field, $\widetilde{E}(k_x, k_y)$ is the Fourier transform of the near-field spatial distribution,

$$\widetilde{E}(k_x, k_y) = \iint E(x, y) \exp[i(k_x x + k_y y)] dx dy \,, \tag{2-1}$$

the field correlation function is then the Fourier transform of the average *k*-vector distribution for an ensemble of random samples [59],

$$\Gamma(\Delta x, \Delta y) = \iint < I(k_x, k_y) > \exp[i(k_x \Delta x + k_y \Delta y)] dk_x dk_y \,, \tag{2-2}$$

where, $< I(k_x, k_y) > = <| \widetilde{E}(k_x, k_y) |^2 >$.

The specific intensity was measured from the spatial distribution of transmitted light in the far-field measured on a CCD detector for an incident collimated beam with a waist of 500-μm diameter. The reason why a 500-μm diameter beam was used is that the angular width of transmitted radiation is seen to be much greater than the divergence of the incident beam but small enough so that the reflection coefficient at individual interfaces is essentially constant as can be seen from measurements of $< I(\theta_x) >$ for different values of $L$ [Fig. 2-6(a)], where $\theta_x = \sin^{-1}(k_x / k)$. The real parts of the corresponding correlation functions, $\Gamma(\Delta x)$, which are Fourier transforms of the measured ensemble average of the specific intensity, are shown in Fig. 2-6(b). The field correlation length [2, 60] of the speckle pattern, $d_\perp$, defined as twice the length in which the real part of the spatial field correlation function decays to a half of its maximum value, is plotted in Fig. 2-8(b).

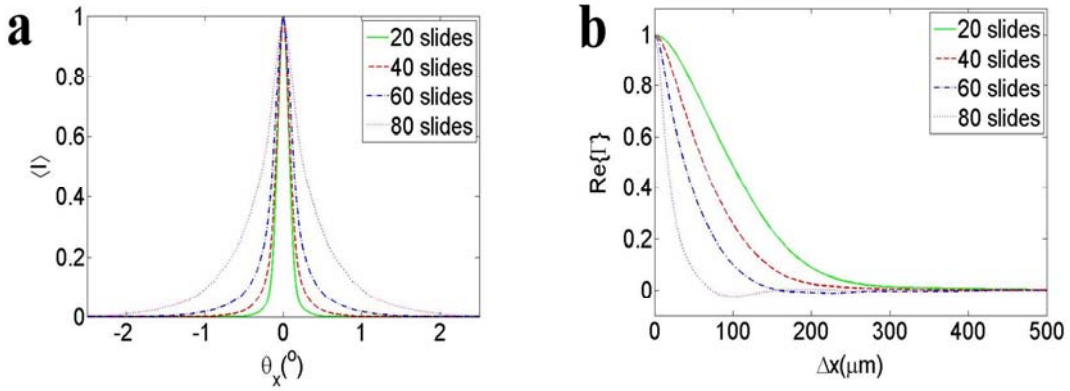


Fig. 2-6 (a) Far-field measurements of the ensemble averaged angular distributions along the *x* direction for an incident Gaussian beam with waist diameter of 500 μm. (b) Real part of the field correlation functions obtained from the Fourier transforms of the specific intensity.

### 2.4.2 Measurement of Transverse Spread of Wave

The ensemble average of the intensity distribution at the output surface, $< I_{out}(x,y) >$, due to an incident beam with intensity profile, $I_{in}(x',y')$, may be expressed in terms of the spread function, $P(x-x',y-y')$,

$$\left\langle I_{out}(x,y)\right\rangle = \iint I_{in}(x',y')P(x-x',y-y')dx'dy'. \tag{2-3}$$

$P(x-x',y-y')$ is similar to the point spread function in three-dimensional diffusive systems but differs in that it depends upon the wave vector distribution at the input since in the layered system the spread increases with the angle of incidence.

Therefore, standard methods used to determine the point spread in three-dimensional random samples such as the direct measurement of the beam profile due to a strongly focused incident beam [61] or the measurement of the intensity correlation function in the far field as a function of sample angle [62, 63] cannot be applied in layered samples. Direct measurement of $I_{in}(x', y')$ and $< I_{out}(x, y) >$ made by imaging the wave onto a CCD camera with a collimated 300-μm diameter incident beam are shown in Fig. 2-7.

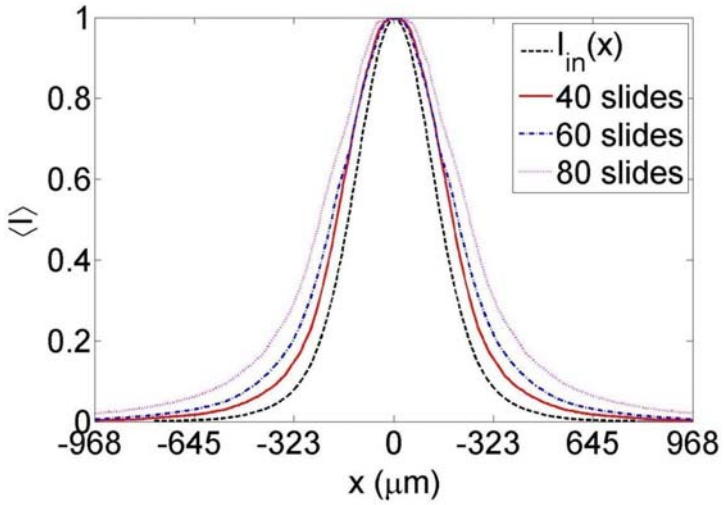


Fig. 2-7 Intensity distributions $I_{in}(x')$ and $< I_{out}(x) >$. The incident Gaussian beam with waist diameter of 300 μm is narrow enough so that the lateral spread of the wave can be determined for $L \geq 30$.

Integrating over $y$ gives $I_{in}(x') = \int I_{in}(x', y')dy'$. Defining $\sigma^2_{x_{in}}$, $\sigma^2_{x_{out}}$ and $\sigma^2_x$ as the variances of the functions, $I_{in}(x')$, $< I_{out}(x) >$ and $P(\Delta x)$, respectively, and taking the origin as the center of the incident beam, gives, $\sigma^2_{x_{in}} = \int I_{in}(x')x'^2 dx'$, $\sigma^2_{x_{out}} = \int < I_{out}(x) > x^2 dx$ and $\sigma^2_x = \sigma^2_{x_{out}} - \sigma^2_{x_{in}}$. The variance so obtained can be used to characterize the spread of the wave in the $x$ direction and is shown in Fig. 2-8(b).

### 2.4.3 Comparison of Coherence Length and Transverse Spread

The variations of the widths of the intensity spread functions and the coherence length along the $x$ direction as a function of the number of cover slips are shown in Fig. 2-8(b). Results for $\sigma_y$ and $d_y$ along the $y$-direction are very close to those found along the $x$-direction. The crossing of the curves for $\sigma_\perp$ and $d_\perp$ marks a crossover from 1D to 3D transport. Such a crossing occurs at $L \approx 35$ in both the $x$- and $y$-directions. Beyond this thickness, $< T(L) >$ departs noticeably from 1D simulations [Fig. 2-3]. Wave localization is essentially 1D only as long as the area explored by a wave incident at a point is smaller than the coherence area of the field. One-dimensional localization breaks down once the sample is thick enough so that the characteristic length of the transverse spread of the wave, $\sigma_\perp$, exceeds the field correlation length in the plane, $d_\perp$, i. e. $\sigma_\perp > d_\perp$.

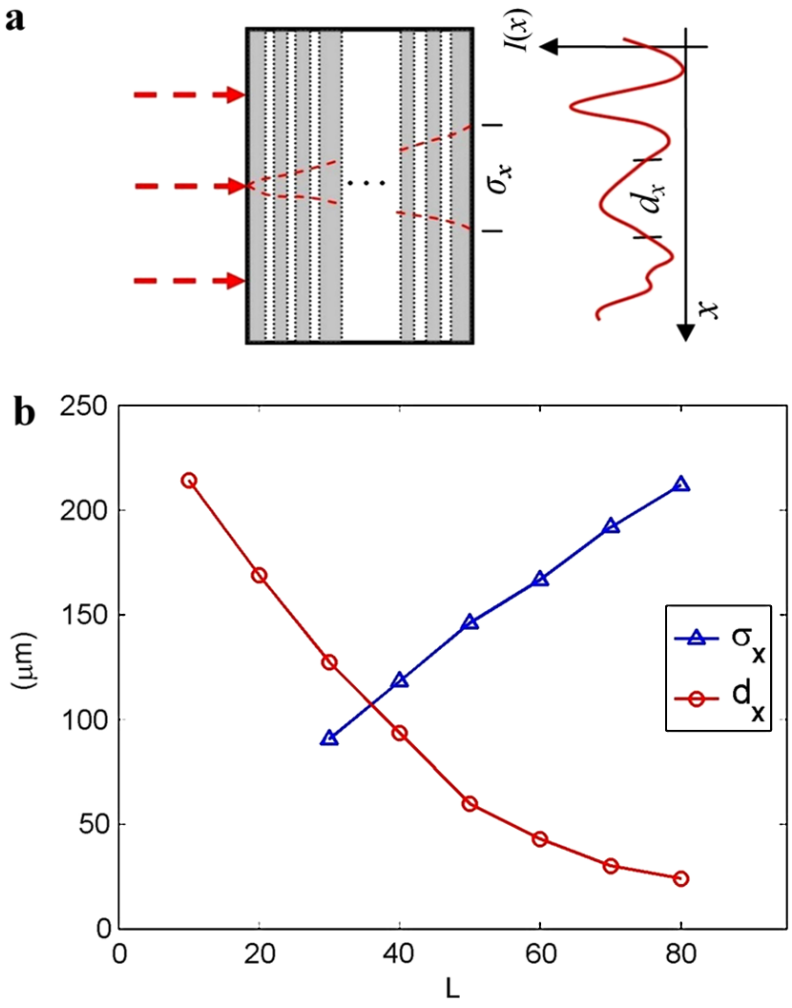


Fig. 2-8 (a) Schematic of the average transverse spread $\sigma_x$ and the speckle size $d_x$ along the $x$ direction at the output plane for an incident plane wave. (b) Measurement of $\sigma_x$ and $d_x$ versus $L$. These curve cross at $L \approx 35$, the same thickness at which departure of $< T(L) >$ from 1D simulations are seen [see Fig. 2-3].

Measurements of $\sigma_\perp$ and $d_\perp$ allow us to determine the effective number of transverse modes involved in transmission of the wave over the area over which the wave spreads, $N = N_x N_y$, where

$$N_x = \begin{cases} 1, & \sigma_x / d_x < 1 \\ \sigma_x / d_x, & \sigma_x / d_x > 1 \end{cases} \tag{2-4}$$

and $N_y$ is similarly defined. When $N$ = 1, wave propagation is essentially one-dimensional. Only a single polarization component of the wave is considered here since transmission is highly polarized even for $L$ = 100 [see Fig. 2-9].

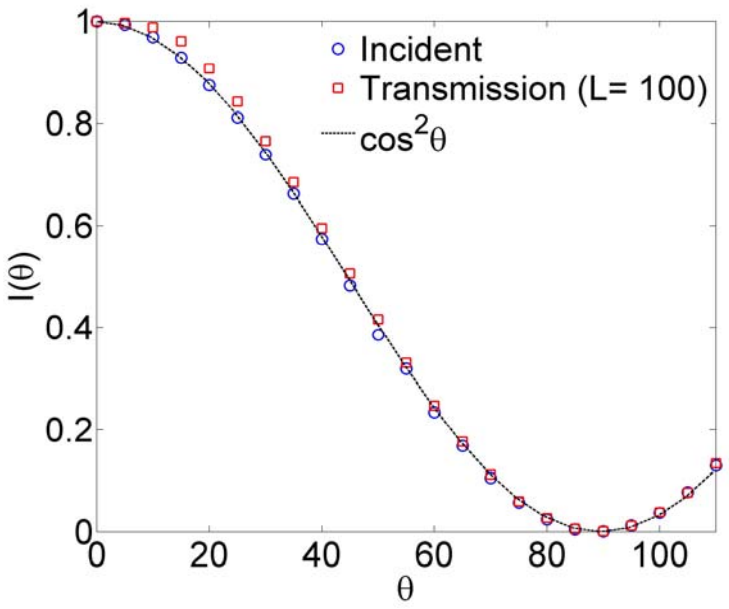


Fig. 2-9 Intensity of the incident beam and transmission for $L$ = 100 through a polarizer versus polarizer angle, $\theta$. Transmission closely follows the $\cos^2\theta$ dependence of polarized light.

# Chapter 3

# Intensity Statistics and Photon Localization in 1D and Beyond

## 3.1 Introduction

The transport of waves in random systems is broadly classified as diffusive or localized [11, 12]. When waves are localized, the averaged transmission is suppressed while relative fluctuations increase with sample size. In nondissipative samples, the scaling and statistics of transmission depend only on the dimensionality of the sample and the ensemble average of the averaged transmission quantity, the dimensionless conductance $g$. In electronic systems, $g = G/(e^2/h)$, where $G$ is the average conductance. The Landauer relation shows that $g$ equals the optical transmittance, $g = \langle T \rangle = \left\langle \sum_{ab} T_{ab} \right\rangle$, where $\langle T_{ab} \rangle$ is the transmission coefficient for an incident transverse mode $a$ into the outgoing mode or a point on the output surface, $b$ [39]. $g$ is a key parameter for localization and localization is achieved for $g < 1$. Once waves are localized, they remain localized if the dimensionality of a sample is fixed. In layered samples, however, which show a dimensional crossover, we see that the degree of localization first increases with sample thickness, $L$, and then decreases.

Transmission statistics in 1D samples with length much greater than the localization length, $L >> \xi$ are predicted to be log-normal. In Q1D, it is possible to

distinguish between the transmittance, $T$, the total transmission, $T_a = \sum_b T_{ab}$, and the transmission coefficient, $T_{ab}$. Since the transmitted wave is thoroughly mixed in Q1D, intensity statistics are uniform across the sample output. The probability distributions of local and integrated intensity at the sample output normalized to their respective ensemble averages, $P(I \equiv s_{ab} = T_{ab} / \langle T_{ab} \rangle)$ and $P(s_a \equiv T_a / \langle T_a \rangle)$, were calculated in the diffusive limit for nondissipative samples and expressed in terms of a single parameter, $g$ [40-42]. Since $\mathrm{var}(s_a) = 2/3g$, the distribution $P(s_a)$ depends only upon its variance. The functional forms of $P(s_a)$ and $P(I)$ were found to be valid even in strongly scattering and dissipative Q1D samples once the "statistical conductance," $g' = 2/3\,\mathrm{var}(s_a)$ is substituted for $g$ as in Eq. (3-6) below [28]. $g'$ scales inversely with $L$ for $g' > 1$ and exponentially for $g' < 1$ [30, 65], as was originally predicted for the localization parameter $g$ [11].

Since dimensionality is crucial to the scaling of statistics [11], a study of transmission statistics in a continuous change of dimension may elucidate the general character of wave propagation in random media. A change of dimensionality with increasing number of slides, $L$, occurs in random layered media with transverse disorder [43]. Measurements of average transmission in stacks of glass cover slips showed a crossover from 1D scaling [54-56] to diffusive scaling [43].

In this Chapter, we present measurements of intensity statistics in random glass stacks in a dimensional crossover from 1D to 3D. In accord with 1D simulations,

the probability distribution of transmission, $P(T)$ vanishes as $T \to 0$ in samples much thinner than the crossover length. 1D simulation shows that $P(T)$ follows a log-normal distribution but falls to zero even faster than the log-normal at low values of $T$. Measurements of $P(I)$ show a transformation from 1D to Q1D statistics, in which $P(I)$ is peaked at $I = 0$, even though the transmitted wave is not limited laterally. This crossover in statistics is associated with a topological transformation of the structure of the transmitted field form 1D to Q1D which exhibits a Gaussian speckle pattern built upon a network of phase singularities at intensity nulls. Beyond the crossover at $L_{co} = 35$, $P(I)$ is found to be a function of a single localization parameter, the "statistical conductance", $g'$ and that localization is achieved for $g' < 1$.

## 3.2 Experiment Setup and Measurements of Spatial Intensity Variation

To measure intensity variation at the output surface of samples, we place the first surface of the sample at the waist of the normally incident 5 mm diameter beam. A tapered optical fiber with mode field diameter of 4 μm was centered in the beam and placed just behind the stack. The signal was detected by a PMT. The sample was translated in the layer plane over a 2×2 $mm^2$ area on a 10 μm grid to yield a spatial variation of intensity equivalent to that for an incident plane wave. For each sample

thickness, spatial variations of intensity were obtained for 10 different arrangements of cover slips.

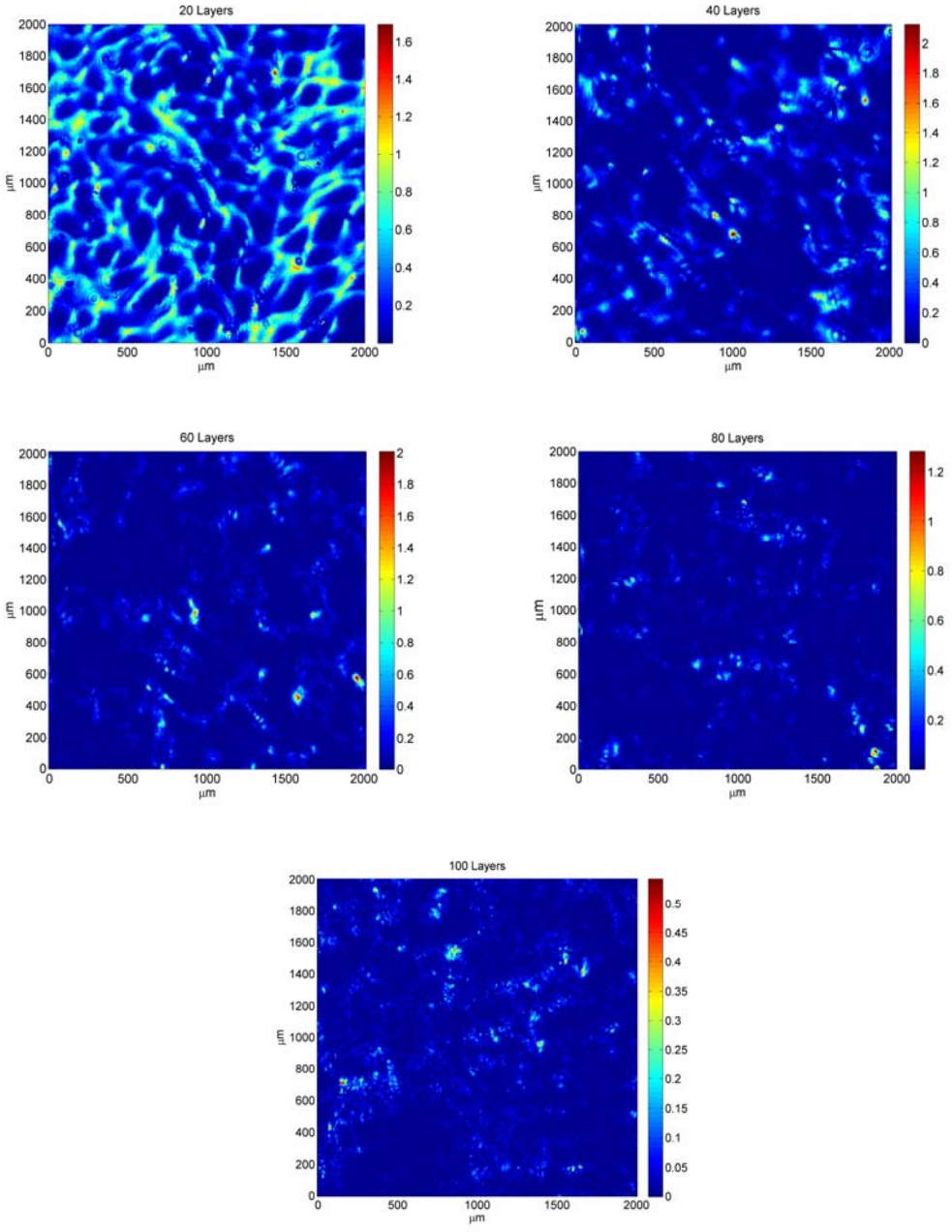


Fig. 3-1 Examples of spatial variation of intensity for 20, 40, 60, 80 and 100 cover slips

Examples of spatial variation of intensity for 20, 40, 60, 80 and 100 cover slips are shown in Fig. 3-1 and 3D images for 20 and 60 cover slips are shown in Fig. 3-2. The average size of bright spots decreases due to the increasing angular spread of transmitted light as the number of slides increases. We see separated sharp peaks in the 3D image for 60 slides which is quite different from the 3D image for 20 slides since the underlying nature of disorder still can be seen in the image for 20 slides unlike the image for 60 slides.

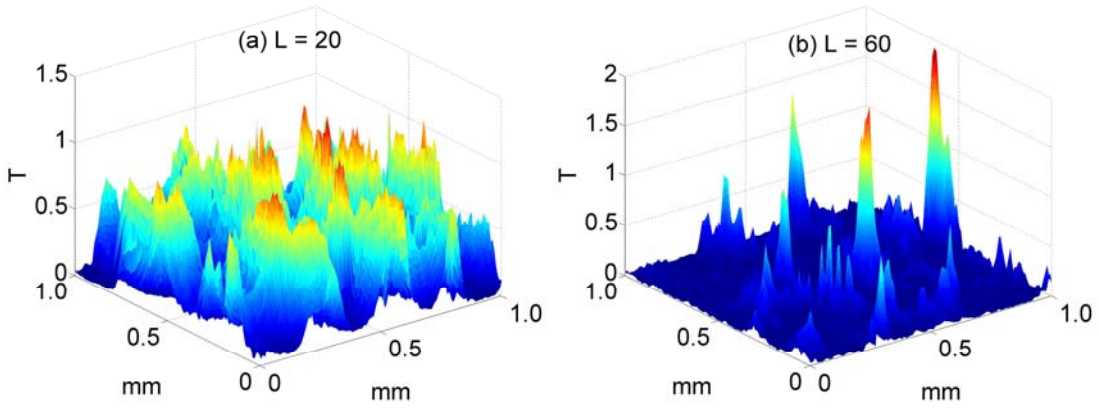


Fig. 3-2 Examples of spatial variation of intensity for (a) 20 and (b) 60 cover slips shown as a 3D image

## 3.3 Spatial Field and Intensity Correlation Function, $F_E(\Delta r)$ and $C(\Delta r)$

From the measured spatial variation of intensity, we can determine the normalized cumulant intensity correlation function, $C(\Delta r) = \langle \delta I(r+\Delta r)\delta I(r) \rangle$, where $\delta I(r) = [I(r) - \langle I(r) \rangle] / \langle I(r) \rangle$, $I(r)$ is the intensity on the output surface of a sample and <...> denotes an average over an ensemble of sample configuration. Macroscopic matrix and diagrammatic calculation in Q1D samples show that the intensity correlation function can be written as a sum of three terms distinguished by the range of correlation [63,73-75],

$$C(\Delta r) = C_1(\Delta r) + C_2(\Delta r) + C_3(\Delta r), \tag{3-1}$$

where, $C_1(\Delta r)$ is short-range correlation, $C_2(\Delta r)$ is long-range correlation and $C_3(\Delta r)$ is infinite-range correlation. The $C_1(\Delta r)$ term arises in the field factorization approximation [76], $C_1(\Delta r) = F(\Delta r) = |F_E(\Delta r)|^2 = |\langle E^*(r+\Delta r)E(r) \rangle|^2$, where $F_E(\Delta r)$ is the field-field correlation function of $E(\Delta r)$, the normalized electromagnetic field on the output surface of a sample. This term dominates intensity fluctuation. The field correlation function $F_E(\Delta r)$ is the Fourier transform of the angular distribution of intensity in the far field [59]. The $C_2(\Delta r)$ term dominates fluctuations in total transmission and the $C_3(\Delta r)$ term is the source of universal conductance fluctuations.

The intensity correlation function in a Q1D sample falls to a constant level corresponding to var($s_a$). In the layered system, however, we see the level of intensity correlation continues to fall with separation between points since the regions within the sample visited by light reaching the two points do not overlap. The intensity correlation function calculated from the Fourier transform of the measured angular distribution of intensity in the far field (see Chapter 2.4), the square of the absolute value of the field correlation function, and the difference between these two correlation functions are shown in Fig. 3-3 for 40, 60, and 60 cover slips.

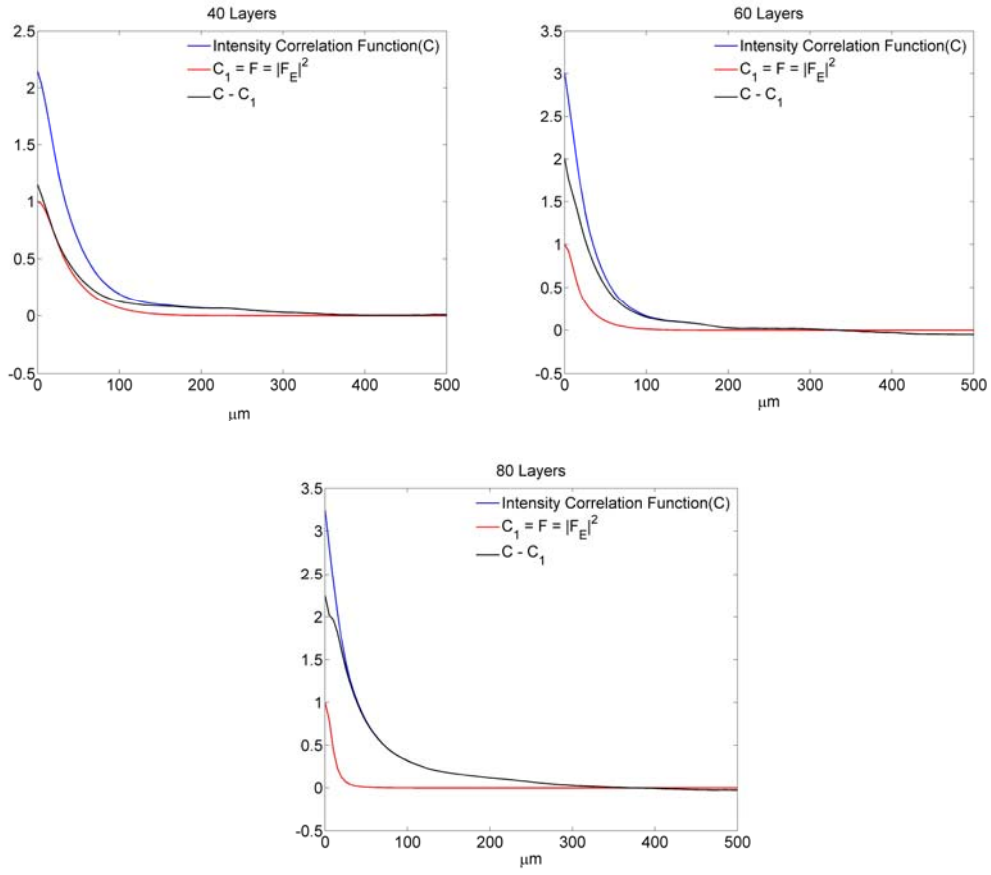


Fig. 3-3 Measured intensity correlation functions and the short- and long-range contributions to correlation for $L$ = 40, 60 and 80

Fig. 3-4 presents the sum of the long- and infinite-range correlation functions for 40, 60, and 60 cover slips. Intensity correlation continuously falls with $\Delta r$. The drop of the correlation function below zero for $\Delta r > 400$ μm is within the noise.

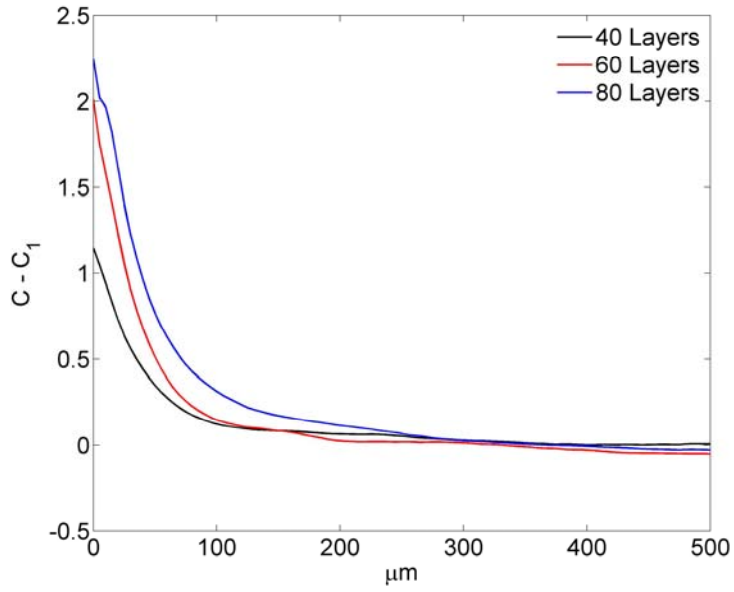


Fig. 3-4 Sum of the long- and infinite-range correlation functions for $L$ = 40, 60, and 80

## 3.4 Variation of Normalized Intensity, $\mathrm{var}(I)$

Measurements of var($I$) versus number of cover slips are shown in Fig. 3-5 and compared to 1D scattering matrix simulations. The measured variance is in excellent accord with 1D simulations in thin samples, but departures can be seen for $L$ > 30. Beyond this thickness, the average transverse spread of the wave, $\sigma_\perp$ exceeds the field correlation length, $1/\delta k_\perp$, where $\delta k_\perp$ is the width of the distribution of $k_\perp$ [43]. Thus, for $\sigma_\perp \delta k_\perp > 1$, wave propagation is no longer determined solely by the longitudinal variation of the index of refraction along a line through the sample, as it would be in 1D, but also reflects lateral scattering due to transverse inhomogeneity.

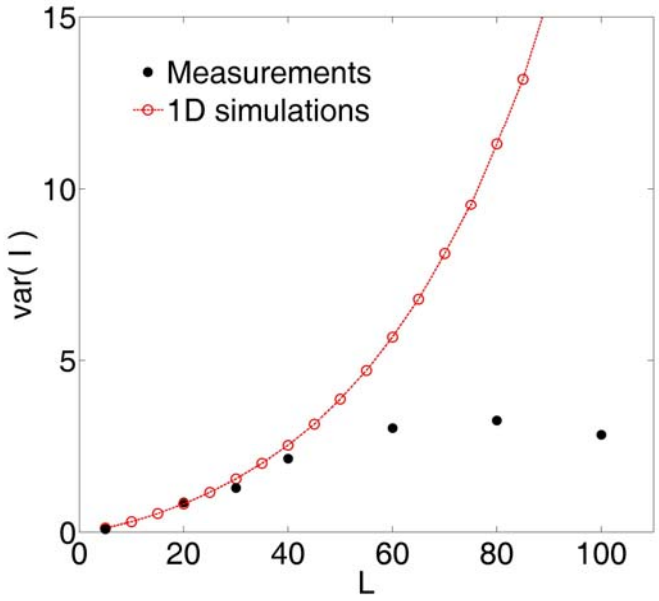


Fig. 3-5 Comparison of scaling of measured var($I$) and 1D simulations

While the simulated results for var($I$) increase exponentially, measurements of var($I$) reach a maximum of 3.2 at $L \sim 80$. This may be compared to the value at the localization threshold in Q1D determined by the condition, $g' = 1$, $\mathrm{var}(I) = 2\,\mathrm{var}(s_a) + 1 = 4/3g' + 1 = 7/3$ [14, 16]. The question arises as to whether the value $g' = 0.61$ inferred from the above relation with $\mathrm{var}(I) = 3.2$ signifies that the wave is localized in the slab geometry of a layered medium. This question can only be addressed by examining the full intensity distribution with increasing $L$ and comparing the results to 1D simulations and to the calculated distribution for Q1D.

## 3.5 Multifractality

A key aspect of the Anderson localization transition in disordered systems is strong intensity fluctuations in space due to the multifractality of wave functions. Multifractality has been studied in various phenomena such as fluid mixing, seismic sequences, rainfall fields, or human heartbeat dynamics. Multifractality in wave functions had been observed in computer simulations and have recently been observed experimentally at the Anderson localization transition in open three dimensional elastic networks [77].

One indication of multifractality in wave functions is that the moments of the probability distribution of inverse participation ratios, $P_q = \int |\Psi(r)|^{2q} d^d r$, where $\Psi(r)$ is the wave function and $d$ is the dimensionality, do not obey conventional

scaling dependence. The dependence can be studied by dividing the system of size $W$ into small boxes of linear size $b$ and varying $b$ where $\sigma << b << W$ and $\sigma$ is the field correlation length. Then, the $q^{\text{th}}$ moment of the inverse participation ratios can be expressed by,

$$P_q = \sum_{i=1}^{n} (I_{B_i})^q = \sum_{i=1}^{n} \left[ \int_{B_i} I(r) d^d r \right]^q , \tag{3-2}$$

where $I(r)$ is the normalized intensity, $I(r) = |\Psi(r)|^2 \Big/ \int |\Psi(r)|^2 d^d r$ , $I_{B_i}$ is the integrated probability inside a box $B_i$ of linear size $b$, and $n = (W/b)^2$ . The ensemble average of the inverse participation ratios shows an anomalous scaling with respect to the dimensionless length $W/b$ at criticality,

$$\langle P^q \rangle \sim (W/b)^{-d(q-1)-\Delta_q} \equiv (W/b)^{-\tau(q)} , \tag{3-3}$$

where, $\tau(q) \equiv D(q-1)$ is the anomalous exponent and $d(q-1)$ , $\Delta_q$ , and $D$ are called the normal, the anomalous, and the fractal dimensions, respectively. The anomalous dimension has an exact symmetry relation, $\Delta_q = \Delta_{1-q}$ [77-79].

Eq. (3-2) is proportional to the moments of the probability distribution of the intensities, so that the scaling relation Eq. (3-3) implies that the probability distribution function of the logarithm of the intensity can be expressed as

$$P(\ln I_B) \sim (W/b)^{-d+f\left(-\ln I_B / \ln(W/b)\right)}, \tag{3-4}$$

where, $f(\alpha)$ is called the singularity spectrum and related to the anomalous exponents $\tau(q)$ by a Legendre transform. In the extended regime, $P(\ln I_B)$ is strongly peaked near $\alpha = d$, while the peak of $P(\ln I_B)$ is shifted from $\alpha = d$ in the localized regime [77].

We obtained the probability distribution function (PDF) in Eq. 3-4 (see Fig. 3-6) from the histogram of the logarithm of box-integrated intensities with the measured spatial variations of intensity on the output surface of stacks of 30, 40, 60, 80, and 100 cover slips shown in Fig. 3-1. The box size chosen of four time larger than the coherence length, $b = 4\sigma$, is larger than the coherence length and smaller than system size. The PDF changes from a distribution strongly peaked at the averaged intensity, $\ln\left(I_B / \langle I_B \rangle\right) = 0$, to much wider distributions shifted from the averaged intensity as the number of layer increases. The PDF for diffusive waves is strongly peaked at the averaged intensity, $\ln\left(I_B / \langle I_B \rangle\right) = 0$, and relatively wide distributions shifted from the averaged intensity for localized waves. It may show photon localization for $L$ = 60, 80 and 100 since the PDF for localized waves is wide distributions shifted from the averaged intensity as shown in Fig. 3-6. We expect that waves will be eventually diffusive as the number of slides keeps increase because of the transverse disorder. We may be able to see a transition from localization to diffusion from the PDF if the spatial variations of intensity are measured for samples thicker than 100 slides.

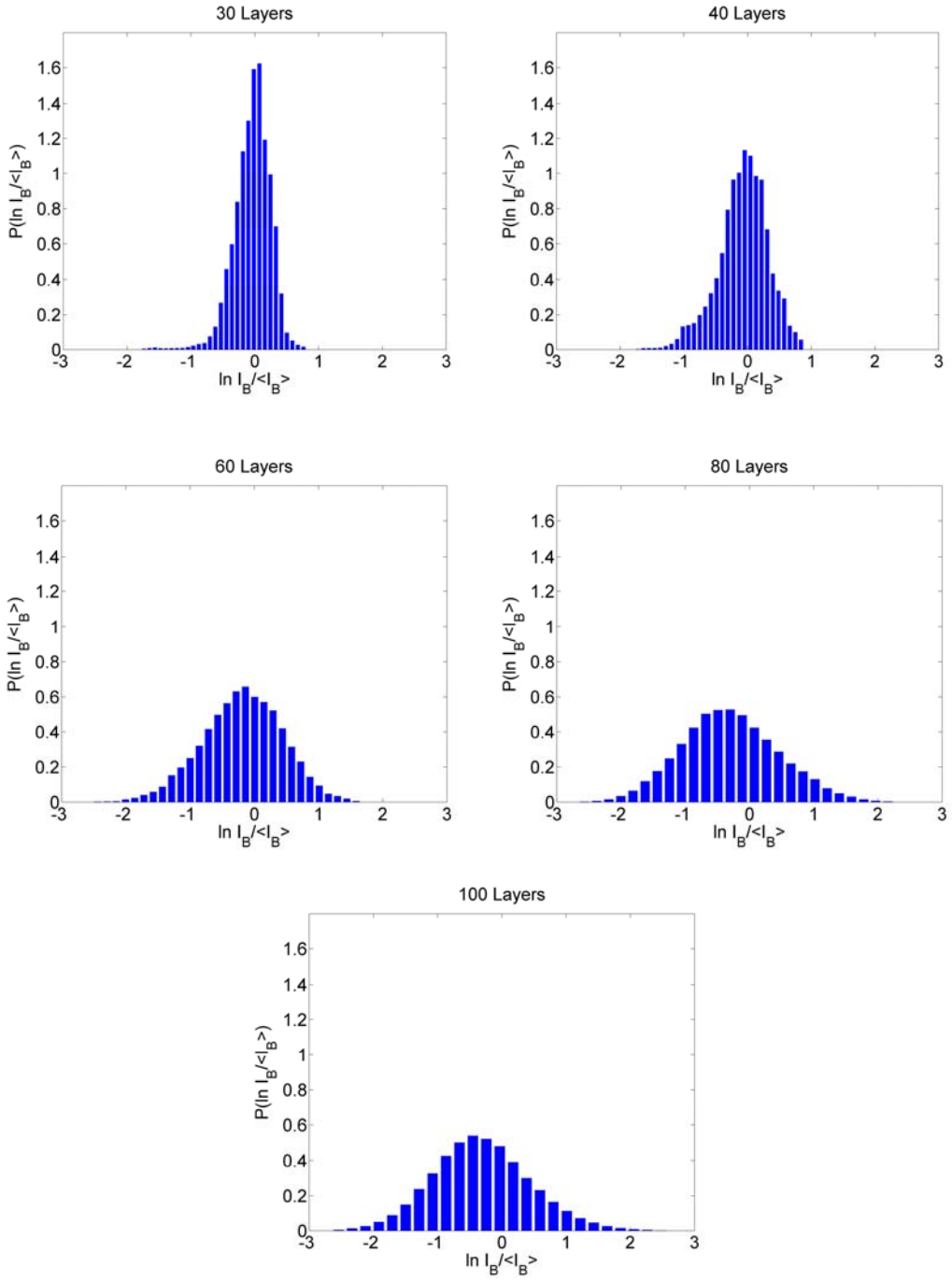


Fig. 3-6 Probability distribution function from the histogram of the logarithm of box-integrated intensities with the measured spatial variations of intensity on output surface of 30, 40, 60, 80, and 100 cover slips

## 3.6 Distribution of Normalized Intensity, $P(s_{ab})$

The relationship between the statistics of $I$ and of $s_a$ in Q1D follows from the statistical independence of $I' \equiv I/s_a$ and $s_a$ and the Gaussian field statistics in single configurations [41, 67]. Fluctuations of intensity in Q1D samples may therefore be represented as a mixture of $P(s_a)$ and $P(I')$. Since $P(I')$ is a negative exponential function for polarized transmission, the intensity distribution is given by,

$$P(I) = \int_0^\infty \frac{1}{s_a} \exp(-I/s_a) P(s_a) ds_a \,. \tag{3-5}$$

The distribution $P(s_a)$ is found from random matrix theory [41] and from diagrammatic [40, 42] calculations in the weak scattering limit in the absence of dissipation to be a function of a single parameter $g$. The distribution has been found to apply even when absorption is present and the wave is localized once $g' = 2/3 \,\mathrm{var}(s_a)$ is substituted for $g$ in the expression for $P(s_a)$ [28],

$$P(s_a) = \frac{1}{2\pi i} \int_{-i\infty}^{i\infty} \exp(q s_a) F(q/g') dq, \tag{3-6}$$

$$F(q) = \exp[-g' \ln^2(\sqrt{1+q} + \sqrt{q})] \,. \tag{3-7}$$

Measurements of $P(I)$ in layered samples are shown for $L$ = 20, 30, 60, 80 and 100 in Fig. 3-7 and compared to 1D simulations and to Eq. (3-5).

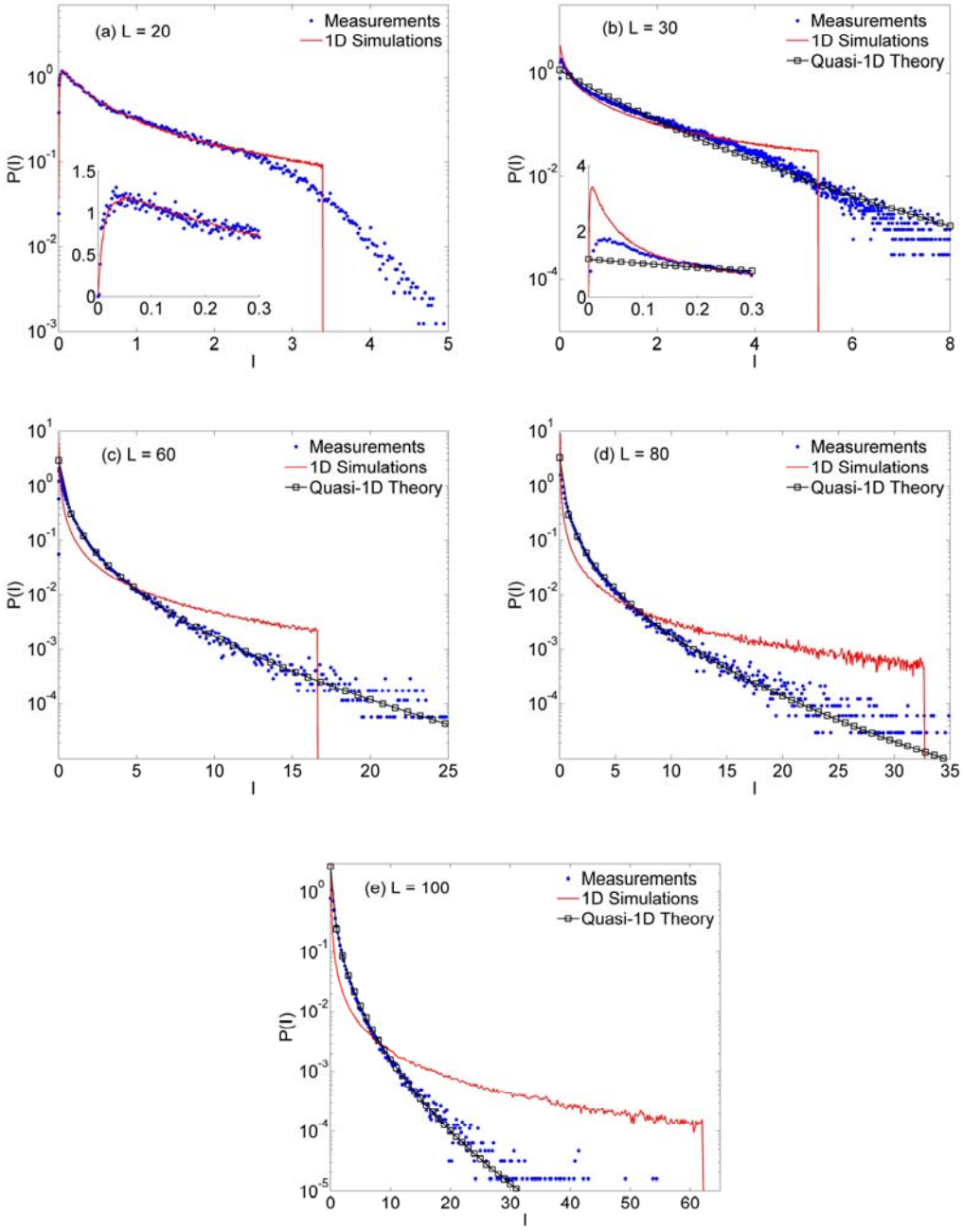


Fig. 3-7 Comparison of measured $P(I = s_{ab})$ to 1D simulations and Eq. (3-5) with same var($I$) for $L$ = 20, 30, 60, 80 and 100. Inserts in the figures for $L$ = 20 and 30 show $P(I)$ for small values of $I$, suggesting that nulls in intensity are absent for $L$ = 20 in agreement of measured $P(I)$ with 1D simulations at $L$ = 20 and demonstrating that measured $P(I)$ falls between 1D simulations and Q1D distribution at $L$ = 30.

$P(I)$ for $L$ = 20 is in excellent agreement with 1D simulations up to $I$ = 2.5. $P(I)$ in 1D simulations vanishes beyond the maximum value of $I$ corresponding to complete transmission, $T_{ab} = 1$, which is 3.4 for $L$ = 20. Higher values of transmission are observed, however, because of the transverse spread of the beam due to nonuniformity in the layers, which does not exist in 1D. The sharp peak of $P(I)$ at low values of $I$ reflects inhibited transmission for localized waves. Below this peak, $P(I)$ drops precipitously towards zero as can be seen in the inset in Fig. 3-7(a).

The absence of nulls in transmission is a distinctive feature of 1D and follows from the finite transmission coefficient for flux through the $i/i+1$ interface between parallel layers, $4n_i n_{i+1}/(n_i + n_{i+1})^2$. This guarantees that the component of flux propagating towards the sample output in any layer does not vanish if it is nonzero in the preceding layer. The vanishing of $P(T)$ at $T$ = 0 can also be seen by comparing $P(T)$ to the log-normal distribution, which is predicted only for $L >> \xi$ [68-70]. The average localization length, $\xi$, or decay rate of $< \ln T(L) >$ in Fig. 3-8 is found to be 11.4 slides [54]. We see in Fig. 4-2 that the bulk of $P(I)$ coincides with a segment of a log-normal distribution even for $L = 3 < \xi$. The distribution of conductance was calculated by Abrikosov for a Gaussian random 1D potential for non-interacting electrons and is also shown in Fig. 4-2. For the log-normal function, $\lim_{T\to 0} P(T) = 0$. 1D simulations in Fig. 4-2 show, however, that $P(T)$ drops even more sharply to zero than a log-normal function or the prediction by Abrikosov. However, intensity

nulls with a associated speckle pattern can occur in layered samples as a consequence of the non-parallelism of the layer interfaces.

For $L$ = 30, $P(I)$ is seen in the inset of Fig. 3-7(b) to fall between the 1D and Q1D distributions, whereas $P(I)$ for $L$ = 60, 80 and 100 [Figs. 3-7(c-e)] are in agreement with Eq. (3-5) with, $g' = 4/3[\mathrm{var}(I) - 1]$, except at the smallest values of $I$. Small values of $I$ could not be measured accurately in thick samples because of the finite detection area set by the mode field diameter of the tapered optical pickup fiber. As a result, the integral of intensity over the mode field area will be larger than the lowest value of intensity in this area.

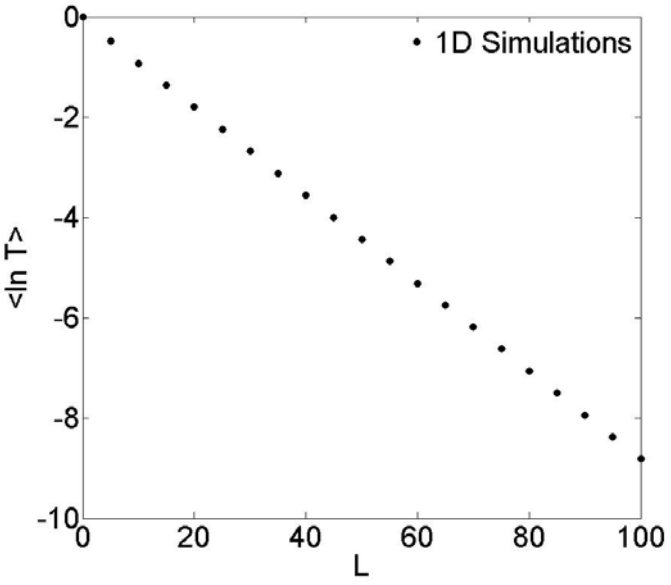


Fig. 3-8 Plot of 1D simulations of $< \ln T(L) >$ versus number of glass cover slips, $L$.

The agreement with Eq. (3-5) with measurements in a layered sample is surprising in view of a key assumption made in its derivation that incident waves are completely mixed at the output of the sample, is violated in the slab geometry. In our samples, the wave is not confined laterally and the mixture of waves from different points on the input of the sample varies along the output. In addition, $P(I)$ in Eq. (3-5) is expressed through the distribution of $s_a$, which is well-defined for the fixed cross sectional area in Q1D, but not in the slab geometry. This can be seen in Fig. 3-9(a), which compares the distribution of $P(s_a)$ calculated from Eqs. (3-6) and (3-7) using the value of $g'$ inferred from the measurements of var($I$) to distributions of integrated transmission through a number of different circular areas at the output of the sample with $L$ = 60. None of the curves for integrated transmission correspond to the calculated distribution.

We therefore treat $s_a$ as a variable of integration in Eq. (3-5) rather than a random variable. $P(I)$ is then a function of a single variable, $g'$, which is a generalized measure of mesoscopic fluctuations and does not have a direct quantitative association with the statistics of integrated transmission. Agreement of $P(I)$ with an expression obtained from Q1D theory for $L > L_{co}$ suggests that, as in Q1D, $P(I)$ reflects statistically independent mesoscopic and Gaussian fluctuation. We tested to see whether the distribution of intensity at a point normalized by its average over an appropriate area surrounding the point may also be negative exponential as is the case in Q1D for a single polarization component. We expect that

such an area will be of the order of magnitude of the intensity correlation area. We find that when the measured intensity is normalize by the average intensity in an area $4\pi R_c^2$, where $R_c$ = 23 μm is the length on which the correlation function falls to half its peak value [see Fig. 3-3(b)], $P(I') = \exp(-I')$, as shown in Fig. 3-9(b). This supports the conjectures that for $L > L_{co}$ the intensity distribution is the same as that given by Gaussian statistics and that $P(I)$ is therefore a mixture of a non-ergodic mesoscopic function and an exponential function. This suggests further that $P(I)$ at $L$ = 30 is not given by Eq. (3-5) because the density of singularities has not reached the generic density of Gaussian speckle patterns [71, 72].

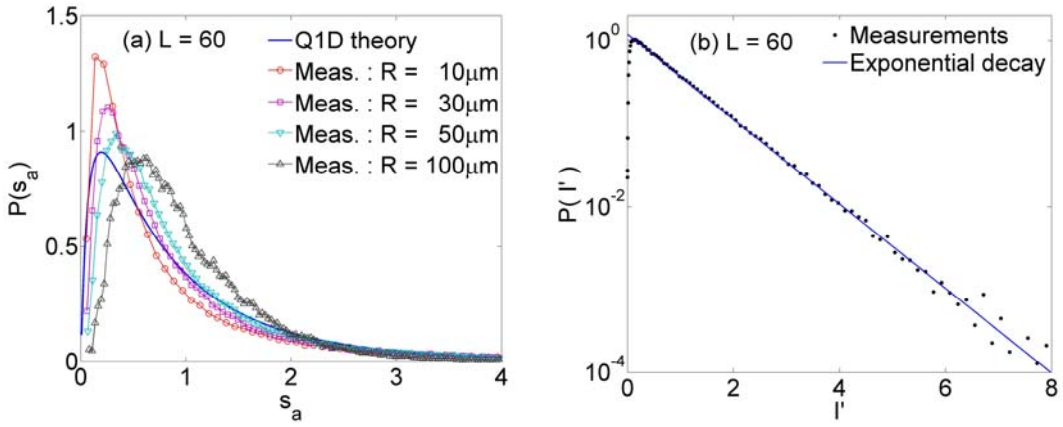


Fig. 3-9 (a) Probability distribution of transmitted intensity integrated over circular areas with different radii for $L$ = 60. The results are compared with $P(s_a)$ given by Eq. (3-6). (b) Probability distribution of transmitted intensity normalized by average intensity in a circle with radius of $2R_c$.

Previous studies in Q1D have indicated that $g'$ defined in terms of var($s_a$) scales as expected for a localization parameter even in the presence of absorption [28, 30]. We expect this will be true as well for $g'$ defined in terms of var($s_{ab}$) for all dimensions beyond 1D. Thus $g' < 1$ demonstrates that in our sample the wave is localized.

# Chapter 4

# 1D Theory and Numerical Simulations

In Chapter 3, the probability distributions of normalized intensity calculated by the scattering matrix method were compared with 1D theory. In this Chapter, the statistics of transmission in 1D will be presented in greater detail.

First of all, the transfer matrix and the scattering matrix methods for calculating the reflection and transmission in multilayer systems will be shown. Then, 1D theory studied by Abrikosov will be introduced and compared with the log-normal distribution and 1D simulations. In addition, the variation of the Lyapunov exponent with thickness and the localization length will be discussed.

3D simulations for the layered systems in which the layers are not uniform are not possible in the present because the sample size is so much larger than $(\lambda)^3$. To get some insight into transport in the layered system, we carried out two simplified simulations. In one, the transmitted intensity was calculated using a 1D simulation but with a variations with displacement in the plane of the sample of the indices along a line through the sample obtained from a model for the nonuniformity of the layers corresponding to the stack of wedged layers. We also calculated incoherent propagation of photons using a Monte Carlo simulation of photons in which the wave aspect of the problem is ignored. This may relate to the diffusive limit of a thick stack

in which the field is incoherent but the angular spread is still small enough that the reflection coefficient at the interfaces is the same for light normally incident upon the interface. Using this model, we find the transverse variation of intensity and the angular spread of the beam.

## 4.1 1D Simulations

The transfer matrix method and scattering matrix method are often used to study reflection and transmission of an electromagnetic field normally incident on a layered system. The numerical transfer matrix calculations are not stable for large multilayered systems. The scattering matrix method is more stable. The two methods will be described below.

Let us consider a general $N$-layer system which has $N$+1 interfaces because there are $N$ layers and 2 background layers ($N$ can be expressed in terms of $L$, $N = 2L - 1$, where $L$ is the number of glass slides). The incident electric wave travels to the right side. Fig. 4-1 shows the notation for the electric field within the system. The subscripts indicate the layer in the layer system, and the + and – signs indicate right and left propagating waves, respectively. $n_j$ is the refractive index and $d_j$ is the thickness of the layer. Note that, for convenience, the electric fields at the right and left sides of the interface are indicated as $E_j^{\pm} e^{\pm ikn_j d_j}$ and $E_j^{\pm}$, respectively. The

exponential terms in the electric fields at the right side of the $N$+1[th] interface are for the sake of uniformity with those at other interfaces, while $d_{N+1}$ should be zero.

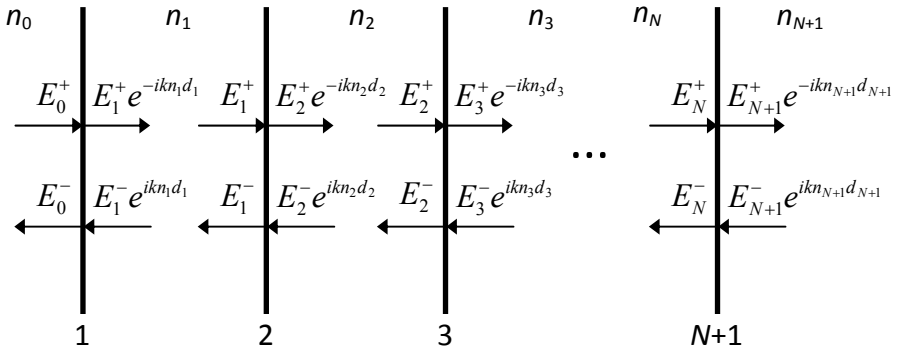


Fig. 4-1 Notation for electric fields within an arbitrary $N$-layer system. The subscripts indicate the layer in the multilayer system, and the + and – signs indicate right and left propagating waves, respectively. $n_j$ is the refractive index and $d_j$ is the thickness of the layer.

When an electromagnetic field propagates from a medium of a given refractive index $n_j$ into a medium of a given refractive index $n_{j+1}$ at the $j$+1[th] interface, part of the incident field is reflected and the rest is transmitted. The reflected and transmitted part of the incident field normalized by the incident field, called the coefficient of reflection $r$ and the coefficient of transmission $t$, respectively,

are calculated from the boundary condition that the electric and magnetic field is continuous at the interface,

$$\begin{aligned} r_{j,j+1} &= \frac{n_j - n_{j+1}}{n_j + n_{j+1}} \\ t_{j,j+1} &= \frac{2n_j}{n_j + n_{j+1}} \end{aligned} . \qquad (4\text{-}1)$$

And, the reflection and transmission are defined as the parts of the incident energy flux that are reflected and transmitted, respectively, and are denoted by $R$ and $T$, respectively,

$$\begin{aligned} R_{j,j+1} &= \left| r_{j,j+1} \right|^2 \\ T_{j,j+1} &= \frac{n_{j+1}}{n_j} \left| t_{j,j+1} \right|^2 \end{aligned} . \qquad (4\text{-}2)$$

### 4.1.1 Transfer Matrix Method

The electric field at the $j^{\text{th}}$ interface will be written as,

$$\begin{aligned} E_j^+ e^{-ikn_j d_j} &= t_{j-1,j} E_{j-1}^+ + r_{j,j-1} E_j^- e^{ikn_j d_j} \\ E_{j-1}^- &= r_{j-1,j} E_{j-1}^+ + t_{j,j-1} E_j^- e^{ikn_j d_j} \end{aligned} . \qquad (4\text{-}3)$$

These equations can be rewritten in matrix form as,

$$\begin{pmatrix} e^{-ikn_j d_j} & -r_{j,j-1} e^{ikn_j d_j} \\ 0 & t_{j,j-1} e^{ikn_j d_j} \end{pmatrix} \begin{pmatrix} E_j^+ \\ E_j^- \end{pmatrix} = \begin{pmatrix} t_{j-1,j} & 0 \\ -r_{j-1,j} & 1 \end{pmatrix} \begin{pmatrix} E_{j-1}^+ \\ E_{j-1}^- \end{pmatrix} . \qquad (4\text{-}4)$$

Then, since $t_{j-1,j}t_{j,j-1} - r_{j-1,j}r_{j,j-1} = 1$, the electric fields $E_j^{\pm}$ at the left side of $j$+1$^{\text{th}}$ interface can be calculated from the electric fields $E_{j-1}^{\pm}$ at the left side of $j^{\text{th}}$ interface,

$$\begin{pmatrix} E_j^+ \\ E_j^- \end{pmatrix} = M_j \begin{pmatrix} E_{j-1}^+ \\ E_{j-1}^- \end{pmatrix}. \tag{4-5}$$

Here, we define the transfer matrix at the $j^{\text{th}}$ interface as,

$$M_j \equiv \begin{pmatrix} \dfrac{1}{t_{j,j-1}} e^{ikn_j d_j} & \dfrac{r_{j,j-1}}{t_{j,j-1}} e^{ikn_j d_j} \\ -\dfrac{r_{j-1,j}}{t_{j,j-1}} e^{-ikn_j d_j} & \dfrac{1}{t_{j,j-1}} e^{-ikn_j d_j} \end{pmatrix}. \tag{4-6}$$

As we see from Eq. (4-5), $E_{N+1}^{\pm}$ can be recursively calculated from $E_0^{\pm}$ with the transfer matrices at every interface, i.e.,

$$\begin{aligned} \begin{pmatrix} E_{N+1}^+ \\ E_{N+1}^- \end{pmatrix} &= M_{N+1} \begin{pmatrix} E_N^+ \\ E_N^- \end{pmatrix} = M_{N+1} M_N \begin{pmatrix} E_{N-1}^+ \\ E_{N-1}^- \end{pmatrix} = \cdots \\ &= M_{N+1} M_N \cdots M_1 \begin{pmatrix} E_0^+ \\ E_0^- \end{pmatrix} \end{aligned}. \tag{4-7}$$

Hence, the transfer matrix for the $N$-layer system can be expressed as the product of the transfer matrices at all interfaces. i. e.,

$$M \equiv M_{N+1} M_N \cdots M_1, \tag{4-8}$$

$$\begin{pmatrix} E_{N+1}^+ \\ E_{N+1}^- \end{pmatrix} = M \begin{pmatrix} E_0^+ \\ E_0^- \end{pmatrix}. \tag{4-9}$$

With $E_{N+1}^{-}=0$, the coefficient of reflection and transmission and the reflection and transmission for the *N*-layer system can be obtained from Eq. (4-9),

$$\begin{aligned} r &\equiv \frac{E_0^-}{E_0^+} = -\frac{M_{21}}{M_{22}} \\ t &\equiv \frac{E_{N+1}^+}{E_0^+} = \frac{M_{11}M_{22}-M_{12}M_{21}}{M_{22}} \\ R &= |r|^2 = \left|\frac{M_{21}}{M_{22}}\right|^2 \\ T &= \frac{n_{N+1}}{n_0}|t|^2 = \frac{n_{N+1}}{n_0}\left|\frac{M_{11}M_{22}-M_{12}M_{21}}{M_{22}}\right|^2 \end{aligned}, \tag{4-10}$$

where $M_{\alpha\beta}$ is the element of the $\alpha^{\text{th}}$ row and $\beta^{\text{th}}$ column of the transfer matrix *M*.

### 4.1.2 Scattering Matrix Method

By regrouping the terms in Eq. (4-3), one readily obtains,

$$\begin{pmatrix} E_j^+ \\ E_{j-1}^- \end{pmatrix} = S(j-1,j)\begin{pmatrix} E_{j-1}^+ \\ E_j^- \end{pmatrix}. \tag{4-11}$$

Here, we define the scattering matrix at the $j^{\text{th}}$ interface,

$$S(j-1,j) \equiv \begin{pmatrix} t_{j-1,j}e^{ikn_jd_j} & r_{j,j-1}e^{2ikn_jd_j} \\ r_{j-1,j} & t_{j,j-1}e^{ikn_jd_j} \end{pmatrix}. \tag{4-12}$$

Note that the scattering matrix relates $E_{j-1}^+$ and $E_j^-$ to $E_j^+$ and $E_{j-1}^-$, i.e., incoming to outgoing electric fields at the interface. This is quite different from that

of the transfer matrix which relates electric fields on one side of the interface to those to the other side. This difference makes the scattering matrix method numerically more stable than the transfer matrix method when the transmission of waves are much smaller than their reflections in a layered system with many layers since $r/t$ terms appeared in the transfer matrix can diverge. Our simulations showed that the transfer matrix method was unstable for samples thicker than 300 layers, while the scattering matrix method remained stable.

From Eq. (4-11), we can write a matrix equation for the entire $N$-layer system,

$$\begin{pmatrix} E_{N+1}^{+} \\ E_{0}^{-} \end{pmatrix} = S(0,N+1) \begin{pmatrix} E_{0}^{+} \\ E_{N+1}^{-} \end{pmatrix}, \tag{4-13}$$

where $S(0,N+1)$ is the complete scattering matrix for the entire $N$-layer system and is what is needed to know the reflection and transmission of the system. To solve this problem, we use the following equation for the $N$-1-layer system,

$$\begin{pmatrix} E_{N}^{+} \\ E_{0}^{-} \end{pmatrix} = S(0,N) \begin{pmatrix} E_{0}^{+} \\ E_{N}^{-} \end{pmatrix}, \tag{4-14}$$

and combine it with the following equation at the $N$+1$^{th}$ interface of the $N$-layer system,

$$\begin{pmatrix} E_{N+1}^{+} \\ E_{N}^{-} \end{pmatrix} = S(N,N+1) \begin{pmatrix} E_{N}^{+} \\ E_{N+1}^{-} \end{pmatrix}. \tag{4-15}$$

From Eqs. (4-14) and (4-15), one readily obtain the following,

$$
\begin{aligned}
E_{N+1}^{+} &= \frac{S_{11}(0,N)S_{11}(N,N+1)}{1-S_{12}(0,N)S_{21}(N,N+1)}E_0^{+} \\
&\quad + \left[ S_{12}(N,N+1) + \frac{S_{12}(0,N)S_{11}(N,N+1)S_{22}(N,N+1)}{1-S_{12}(0,N)S_{21}(N,N+1)} \right] E_{N+1}^{-} \\
E_0^{-} &= \left[ S_{21}(0,N) + \frac{S_{11}(0,N)S_{22}(0,N)S_{21}(N,N+1)}{1-S_{12}(0,N)S_{21}(N,N+1)} \right] E_0^{+} \\
&\quad + \frac{S_{22}(0,N)S_{22}(N,N+1)}{1-S_{12}(0,N)S_{21}(N,N+1)} E_{N+1}^{-}
\end{aligned}
\quad , \quad \text{(4-16)}
$$

where $S_{\alpha\beta}$ is the element of the $\alpha^{\text{th}}$ row and $\beta^{\text{th}}$ column of the scattering matrix *S*. By comparing Eq. (4-16) to Eq. (4-13), we obtain the scattering matrix for the *N*-layer system in terms of the scattering matrices for the *N*-1-layer system and at the $N$+1$^{\text{th}}$ interface,

$$
\begin{aligned}
S_{11}(0,N+1) &= \frac{S_{11}(0,N)S_{11}(N,N+1)}{1-S_{12}(0,N)S_{21}(N,N+1)} \\
S_{12}(0,N+1) &= S_{12}(N,N+1) + \frac{S_{12}(0,N)S_{11}(N,N+1)S_{22}(N,N+1)}{1-S_{12}(0,N)S_{21}(N,N+1)} \\
S_{21}(0,N+1) &= S_{21}(0,N) + \frac{S_{11}(0,N)S_{22}(0,N)S_{21}(N,N+1)}{1-S_{12}(0,N)S_{21}(N,N+1)} \\
S_{22}(0,N+1) &= \frac{S_{22}(0,N)S_{22}(N,N+1)}{1-S_{12}(0,N)S_{21}(N,N+1)}
\end{aligned}
\quad . \quad \text{(4-17)}
$$

$S(0,N+1)$ is calculated from $S(0,N)$ and $S(N,N+1)$ and $S(0,N)$ is calculated from $S(0,N-1)$ and $S(N-1,N)$, etc. Hence, $S(0,N+1)$ can be obtained by recursive calculation from $S(0,1)$ and $S(1,2)$, which is known. The coefficients of reflection and transmission and the reflection and transmission for the *N*-layer system can be obtained from Eq. (4-13) with $E_{N+1}^{-} = 0$,

$$
\begin{aligned}
r &\equiv \frac{E_0^-}{E_0^+} = S_{21}(0,N+1) \\
t &\equiv \frac{E_{N+1}^+}{E_0^+} = S_{11}(0,N+1) \\
R &= |r|^2 = |S_{21}(0,N+1)|^2 \\
T &= \frac{n_{N+1}}{n_0}|t|^2 = \frac{n_{N+1}}{n_0}|S_{11}(0,N+1)|^2
\end{aligned}
\quad . \tag{4-18}
$$

## 4.2 1D Theory

A Gaussian random potential in a 1D non-interacting electron system was studied by Abrikosov. He calculated the probability distribution function of the resistance for arbitrary sample length [68-70],

$$
P(\rho,t) = \frac{2}{\sqrt{\pi t^3}} \int_{x_0}^{\infty} \frac{x}{\sqrt{\cosh^2 x - \rho}} \exp[-(t/4 + x^2/t)] dx , \tag{4-19}
$$

where $x_0 = \cosh^{-1}\sqrt{\rho}$, $t = L/\ell$, $L$ is the sample length, $\ell$ is the mean free path and $\rho$ is the resistance. Since $\rho = 1/T$ in 1D systems based on the Landauer relation, $g = T$, the probability distribution function for the logarithm of transmission is expressed as $P(\ln T, t) = P(\rho,t)\left|d\rho/d\ln T\right| = P(\rho,t)\rho$. In the diffusive regime, $t < 1$, the distribution, $P(\ln T, t)$, reaches a maximum at $\ln T = 0$ and obeys a Poisson distribution. In the deeply localized regime, $t >> 1$, the distribution peaks at $\ln T = -t$ and is a log-normal distribution [69,70],

$$P(\ln T, t) \approx \frac{1}{2\sqrt{\pi t}} \exp\left[ -\frac{(\ln T + t)^2}{4t} \right], \quad t >> 1. \tag{4-20}$$

We obtained the probability distributions of the transmission in 1D from the scattering matrix method and fit these to a log-normal function and 1D theory. 1D simulations show that the bulk of the distribution follows a log-normal distribution even for samples as thin as 3 slides. However, the tail of the distribution at low values of $T$ falls to zero even faster than the log-normal distribution. Fig. 4-2 shows the results of 1D simulations and the best fit of a log-normal distribution and 1D theory to the data.

The log-normal function is defined as,

$$P(\ln T) = \frac{1}{\sqrt{2\pi}\sigma_{\ln T}} \exp\left[ -\frac{(\ln T - \ln T_0)^2}{2\sigma_{\ln T}^2} \right]. \tag{4-21}$$

We see that the peak of the Gaussian functions, $\ln T_0$, shifts to smaller values of $\ln T$ and the variance, $\sigma_{\ln T}^2$, increases as the number of slides increases in Fig. 4-3.

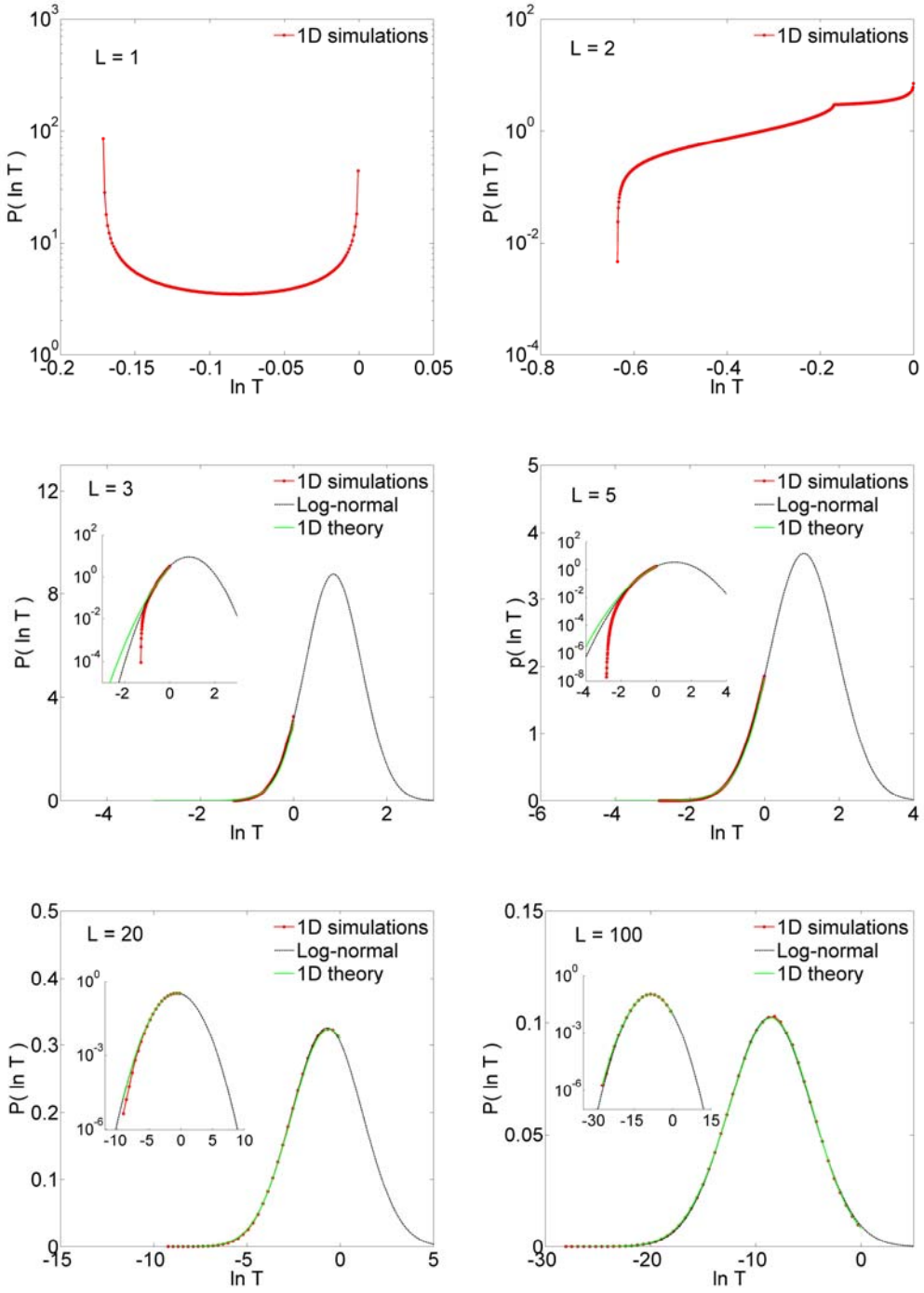


Fig. 4-2 Probability distribution of the transmission in 1D for 1, 2, 3, 5, 20 and 100 slides. The log-normal distributions and 1D theory are fit to 1D simulations. The distributions can be expressed as a segment of a log-normal distribution as long as the sample is thicker than three slides.

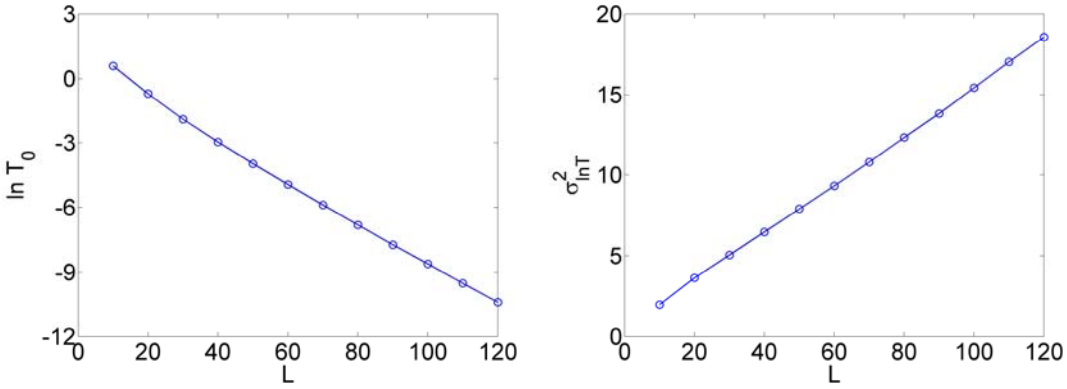


(a) (b)

Fig. 4-3 (a) position of the peak and (b) the variance of the Gaussian function versus number of layers

A major difference between Q1D and 1D is the presence of phase singularities at which intensity vanishes at the output of Q1D samples. Once the density of singularities reaches the value for generic speckle patterns, the intensity follows Q1D statistics. There are no singularities in 1D. A minimum transmission, $T_m$ occurs with a value equal to the transmission in a band gap which specially satisfies the condition, $2n_i d_i = (m+1/2)\lambda$, where $n_i$ and $d_i$ are the refractive indices and thickness of the layers, respectively, and *m* is any positive integer. The minimum transmission decays exponentially with the number of layers (Fig. 4.4).

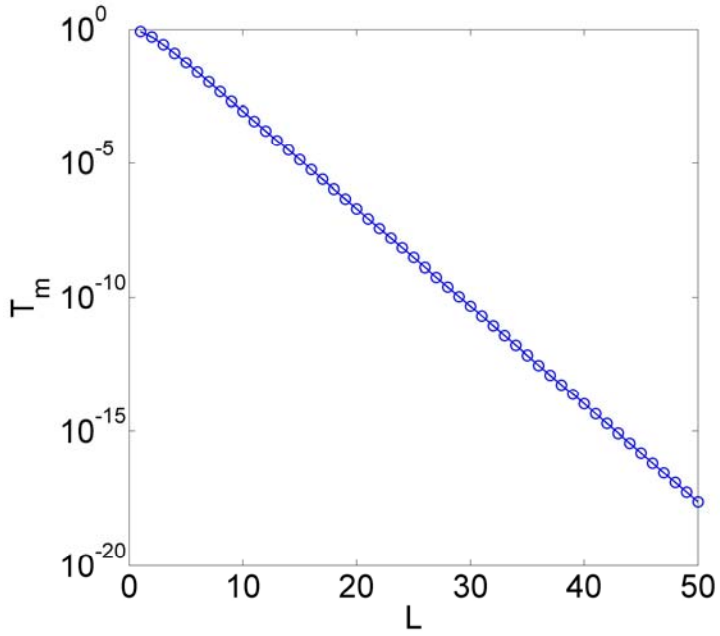


Fig. 4-4 Minimum of transmission in 1D vs. the number of layers.

The longitudinal flux distributions for samples of 5 and 40 slides are shown in Fig. 4.5 in a sample in which transmission is at a minimum. Fig. 4-5(a) and (c) are the forward and backward flux and their sum for samples of 5 and 40 slides. These samples have 11 and 41 layers, respectively, since we used same refractive index, 1, for one layer of the binary system and the background layers. Flux decays exponentially except for the last few layers. Fig. 4-5(b) and (d) show the fractional change of flux passing through each glass layer. In other word, this is the ratio of the

flux after the glass layer to the flux before the layer. Forward flux and backward fluxes are symmetric and their sum is constant except in the last few layers.

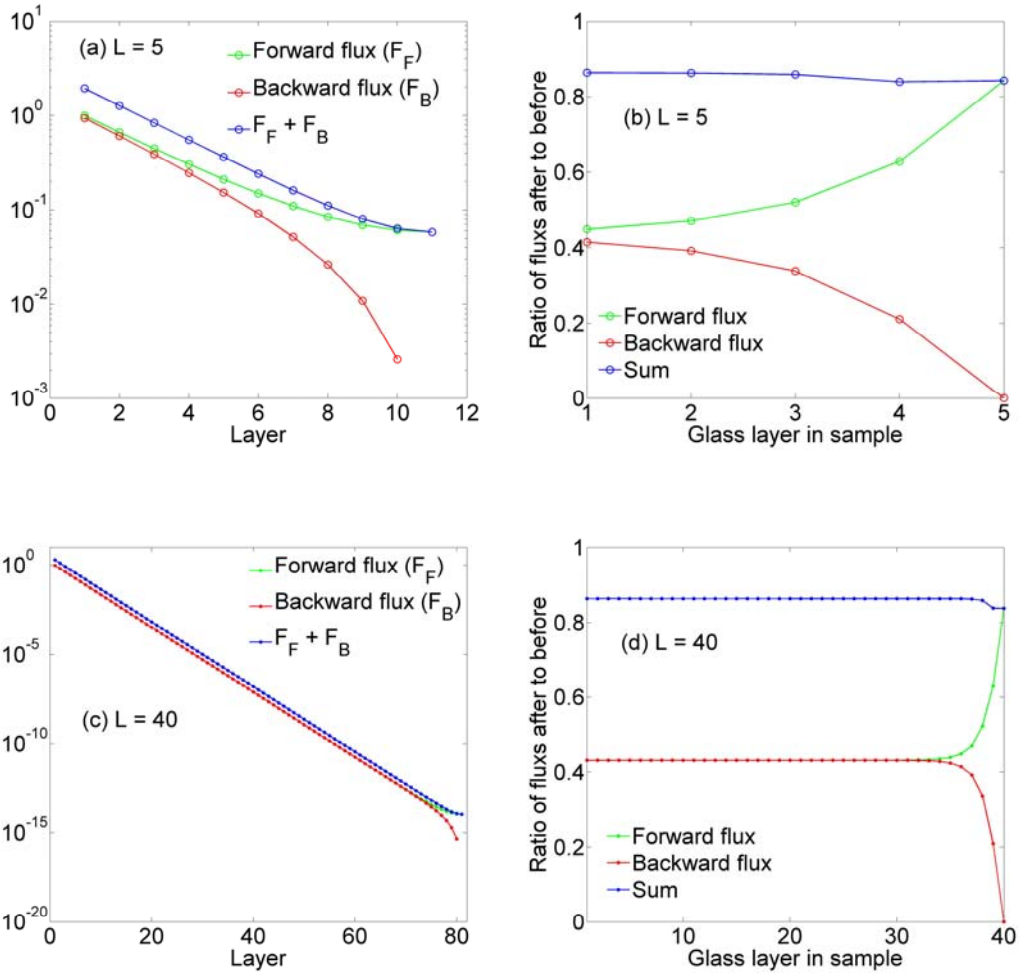


Fig. 4-5 Forward and backward flux distribution for (a) $L$ = 5 and (c) $L$ = 40 at minimum transmission and ratio of flux after glass layer to flux before glass layer for (a) $L$ = 5 and (c) $L$ = 40.

To explore the rapid falloff of the probability distribution near its minimum value, $T_m$, we consider the probability distribution of $\ln(T - T_m)$ for $L$ = 1, 2, 3 and 4 (Fig. 4-6). At low values of $\ln(T - T_m)$, we find $P(\ln(T - T_m)) \sim \exp(\alpha \ln(T - T_m))$ $= (T - T_m)^{\alpha}$. The exponential decay, $\alpha$, increases linearly with the number of slides and does not depend on the refractive index as shown in Fig. 4-7. Then, as number of slides increases, the slope starts to depart from the linear increase with $L$. The departure from linearity is earlier the higher the refractive index.

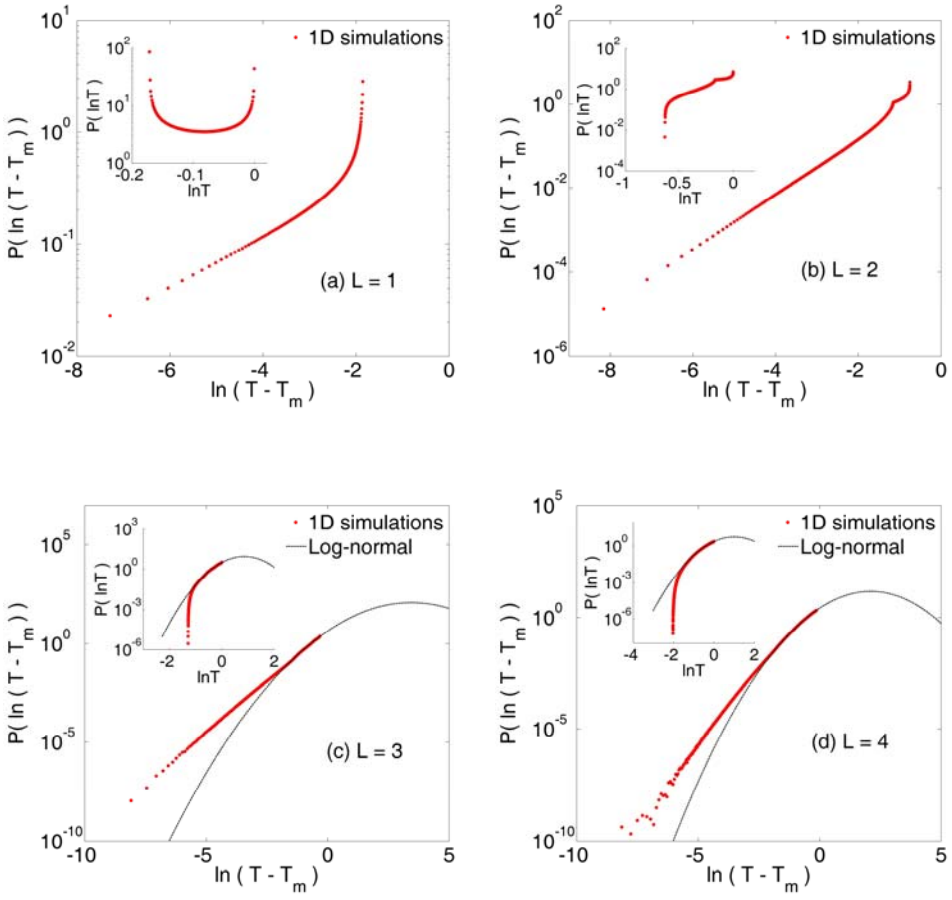


Fig. 4-6 Probability distribution of $\ln(T - T_m)$ for $L$ = 1, 2, 3 and 4.

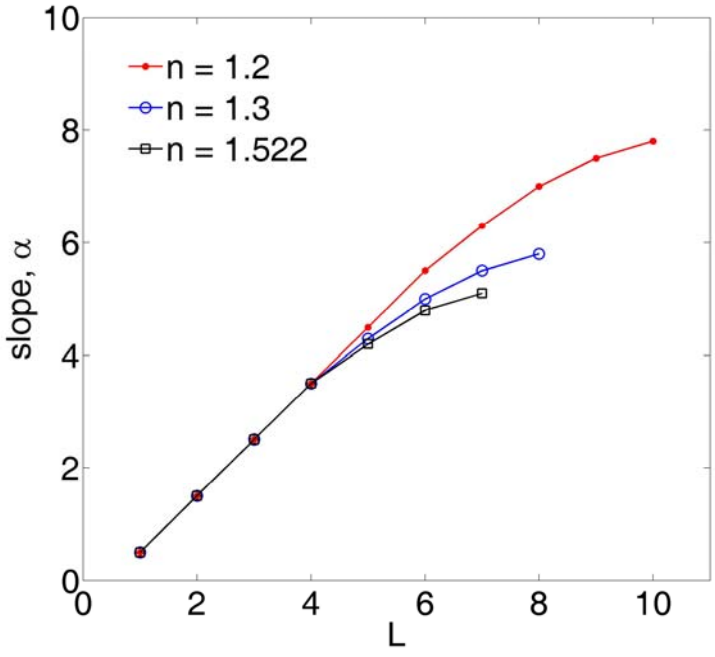


Fig. 4-7 Exponential slope of the distributions, $\alpha$, for low values of $\ln(T - T_m)$ with the number of slides for different refractive indices.

## 4.3 Lyapunov Exponent

The scaling theory of localization suggested that there exist a parameter, the dimensionless conductance *g*, to describe a scaling of *g*(*L*) in a size of a system *L*. It was soon realized that since fluctuations in *g* are large, it would be useful to describe the scaling of an entire distribution of conductance. This was done by considering the

statistics of the Lyapunov exponent $\gamma$ [Eq. (4-22)] [11, 80, 81]. The Lyapunov exponent is defined as,

$$\gamma(L) = -\frac{1}{2L}\ln T(L), \tag{4-22}$$

In the limit $L \to \infty$, the Lyapunov exponent self-averages to $\bar{\gamma}$ and its distribution approaches a Gaussian form. The single parameter scaling (SPS) theory provides a connection between the self-averaged value $\bar{\gamma}$ and the variance $\sigma_\gamma^2$ of the distribution of $\gamma$, which is Gaussian,

$$\sigma_\gamma^2 \frac{L}{\bar{\gamma}} = 1. \tag{4-23}$$

In this section, we consider the distributions of the Lyapunov exponent and Eq. (4-23). The distribution of the Lyapunov exponent is calculated from the distribution of ln*T*. Since the distribution of ln*T* is a segment of a Gaussian function even for samples as thin as 3 slides, the distribution of the Lyapunov exponent, $P(\gamma)$, is also a segment of a Gaussian function,

$$\begin{aligned} P(\gamma) &= P(\ln T)\left|\frac{d\ln T}{d\gamma}\right| = 2LP(\ln T) \\ &= A\exp\left[-\frac{(\gamma + \ln T_0/2L)^2}{2\sigma_{\ln T}^2/4L^2}\right] \\ &\equiv A\exp\left[-\frac{(\gamma-\gamma_0)^2}{2\sigma_\gamma^2}\right] \quad ,0 \le \gamma \le -\frac{1}{2L}\ln T_m \end{aligned}, \tag{4-24}$$

where, $A$ is a normalization constant. Fig. 4-8 shows $P(\gamma)$ for 5, 20, 60 and 100 slides. $P(\gamma)$ is a segment of a Gaussian function which narrows as the number of slides increase.

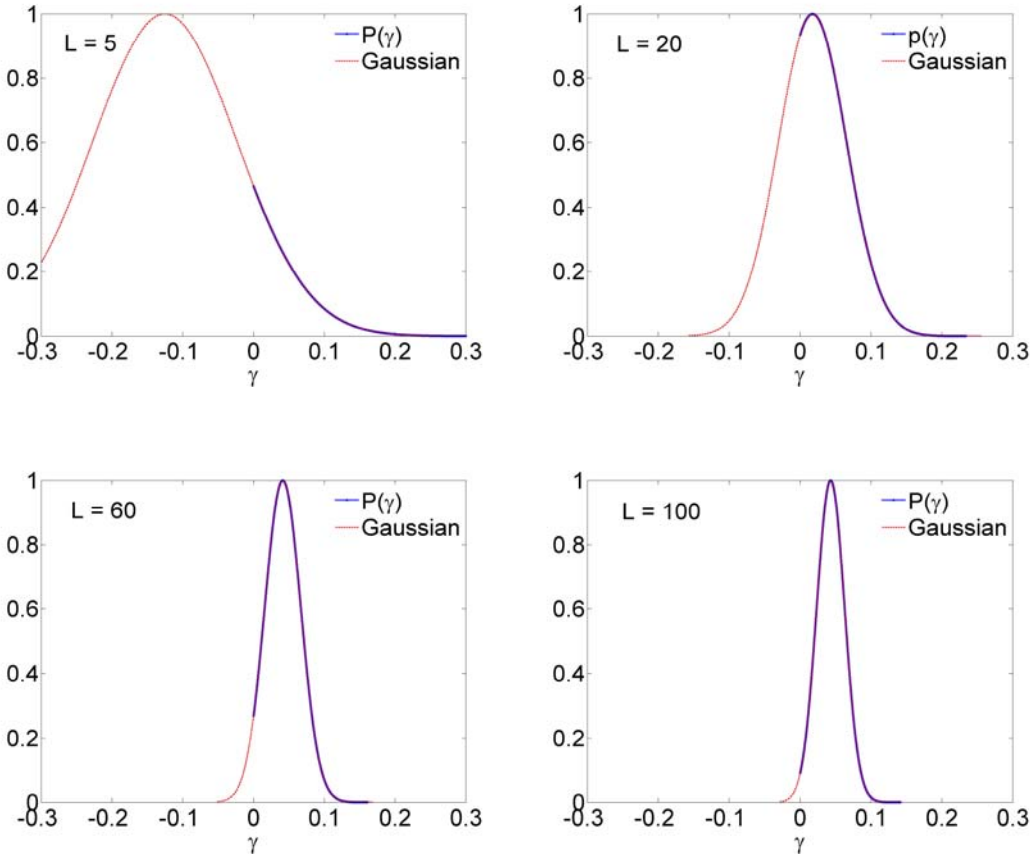


Fig. 4-8 Distribution of the Lyapunov exponent for $L$ = 5, 20, 60 and 100 slides. $P(\gamma)$ is a segment of a Gaussian function and its peak shifts to larger $\gamma$ and becomes narrower as the number of slides increases.

We define $\gamma_0$ and $\sigma_\gamma^2$ as the center and the variance, respectively, of the Gaussian fit for the distribution of the Lyapunov exponent as Eq. (4-24). $\gamma_0$ is compared with the average of $\gamma$ in Fig. 4-9(a). $\langle\gamma\rangle$ is relatively constant and the same as $\gamma_0$ for large $L$. In Fig. 4-9(b), we see the variance of $\gamma$ decreases with the number of slides. Fig. 4-10 is a calculation of Eq. (4-23) with $\gamma_0$ and $\langle\gamma\rangle$ instead of $\bar{\gamma}$. The value calculated with $\langle\gamma\rangle$ is constant as the number of slides changes, although the values approaches 8.9 not one [Eq. (4-23)] as the number of slides increases. $\langle\gamma\rangle$ appears to be directly related with $\sigma_\gamma^2$ even for samples smaller than the mean free path length. We may say the single parameter scaling with $\langle\gamma\rangle$ is valid even for small $L$.

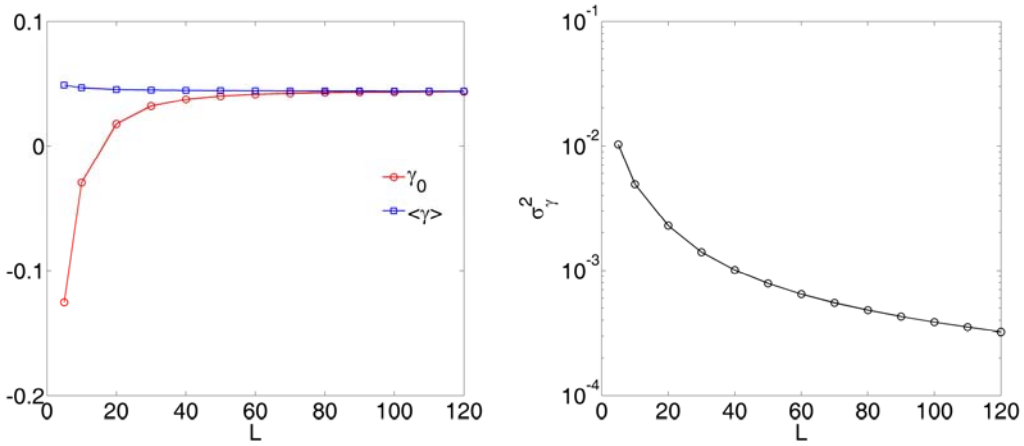


(a) (b)

Fig. 4-9 (a) Comparison of $\gamma_0$ with $\langle\gamma\rangle$ and (b) the variance of $\gamma$ with the number of slides. $\langle\gamma\rangle$ shows a constant with changing the number of slides.

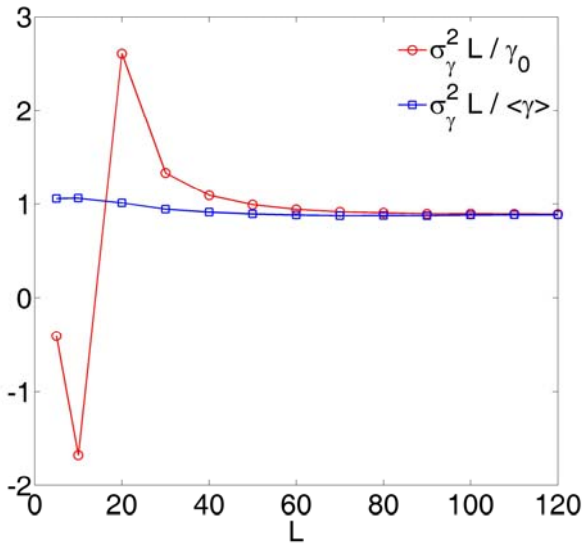


Fig. 4-10 Relations between the variance of $\gamma$ and $\gamma_0$ and $\langle\gamma\rangle$. $\langle\gamma\rangle$ is related with $\sigma_\gamma^2$. The single parameter scaling with $\langle\gamma\rangle$ appears to be valid even for small $L$.

## 4.4 Intensity Pattern

We tried a simple simulation to compute the intensity pattern at the output of the sample. Transverse disorder is introduced via the nonparallel of the glass/air interfaces as described below. The longitudinal variation of index at a point on the transverse plane is directly related to configurations at nearby points on the transverse plane. We assume the reflected and transmitted waves at each interface are normal to the layers. Thus there is no spread of the wave along the transverse direction and no

broadening of the angular distribution of the transmitted wave. Comparing the simulations with the measured intensity patterns allows us to see the impact of the transverse spread and angular distribution of waves on intensity patterns. These simulations are expected to represent the transmitted waves in thin stacks but not for thick stacks.

In Fig. 4-11, simulated intensity patterns on the left for 20, 40 and 60 slides are compared with measured intensity patterns on the right. From the simulations, we see bright spots become smaller and dark areas grow as the number of slides increase and a network of bright lines emerges. Similar behavior can be seen in the measured pattern for 20 slides. As the number of slides increases, however, bright regions in the measured patterns become disconnected and less elongated unlike those on the simulated patterns.

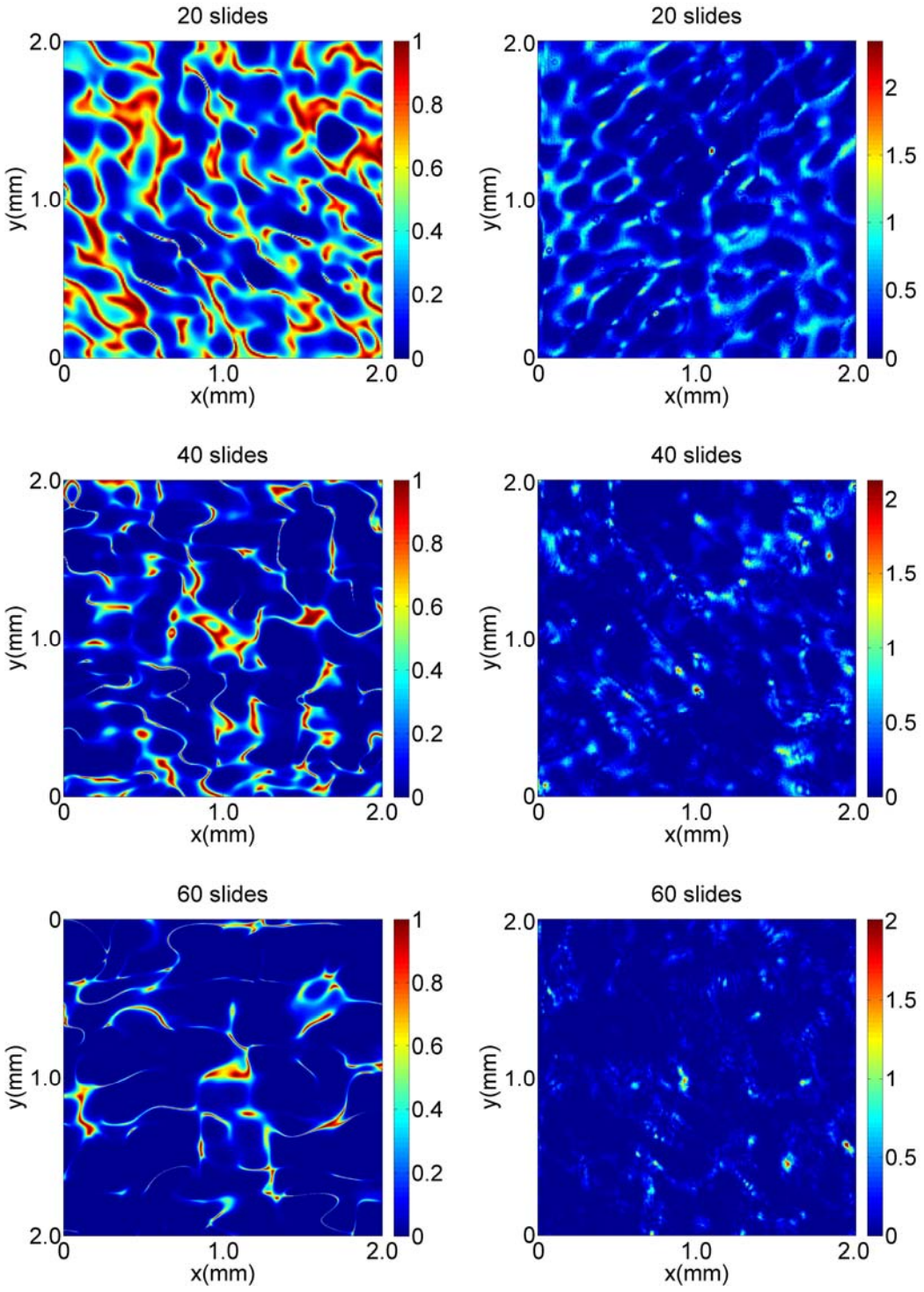


Fig. 4-11 Simulated intensity patterns on the left for 20, 40 and 60 slides are compared with measured intensity patterns for the corresponding number of slides on the right.

## 4.5 Monte Carlo Simulation

Monte Carlo simulation use repeated random sampling based on a proper probability for computing their results. It is especially useful when problems involve a large number of coupled degrees of freedom or when it is impossible to compute exact results using a deterministic algorithm. The distributions of position and angle of transmitted photons in random layered systems with transverse disorder are simulated by repeated random sampling. Transverse disorder is computed for layered systems initially composed of air and glass layers which have same optical thickness. The degree of transverse disorder is expressed in terms of standard deviation of the angle, $\alpha$ , with respect to incident direction of photons. The distributions of position and angle of transmitted photons for 20 and 40 slides with two different transverse disorder, $\alpha$ , are shown in Fig. 4-12. The influence of photon localization on the distribution will be seen in the difference between the Monte Carlo simulations and measurements if the transverse spread function is measured in the layered systems with same transverse disorder in the simulations.

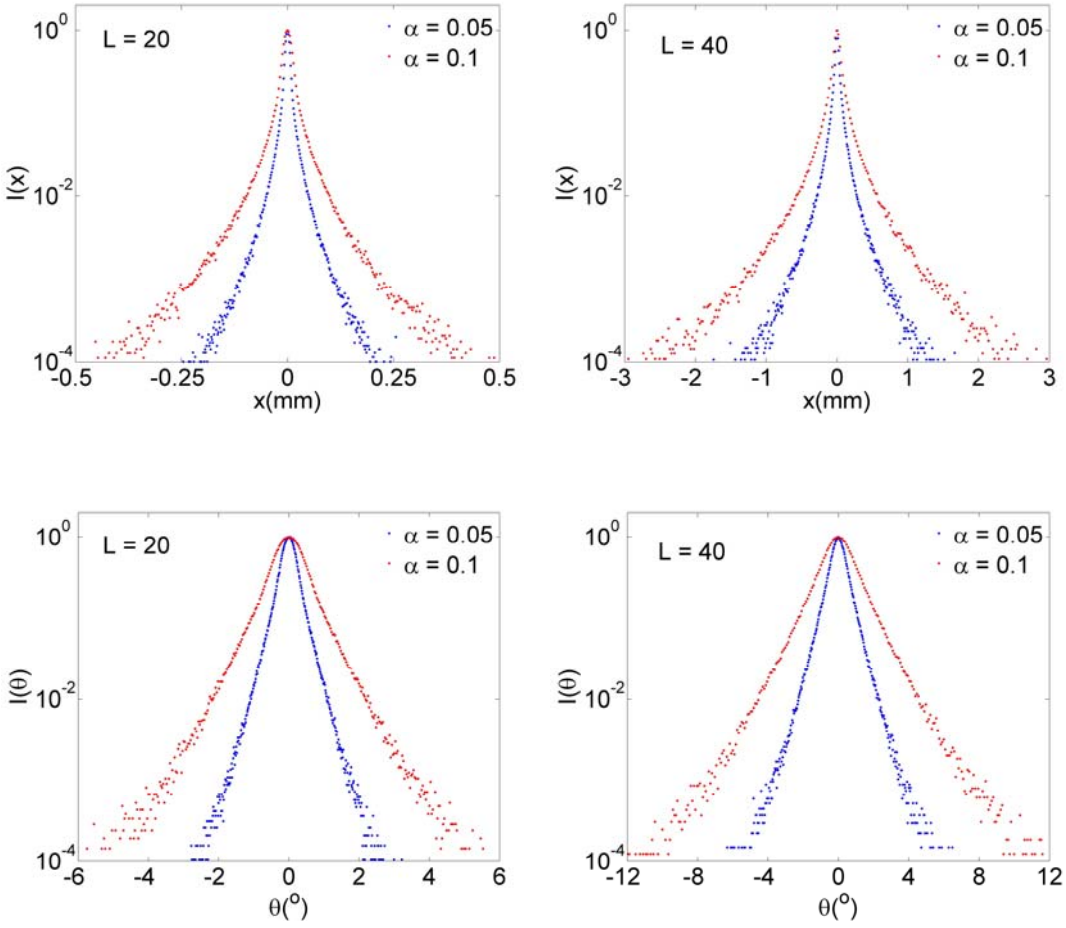


Fig. 4-12 Monte Carlo simulation results of distribution of position, $I(x)$, and distribution of angle, $I(\theta)$, at output surface of the systems for 20 and 40 slides with transverse disorder, $\alpha$.

# Chapter 5

# Conclusion

The scaling and statistics of transmission in layered samples differs from the scaling and statistics in samples in which wave propagation is of fixed dimensionality. In such samples, the wave, once localized, remains localized, and the dimensionless conductance or diffusion coefficient falls continuously for samples with dimensionality $d < 2$ and increases with sample length for diffusive 3D samples. In contrast, longitudinal delocalization and a dimensional crossover from 1D to 3D are observed in the layered samples.

We find a transition from localization towards eventual diffusion with increasing thickness and disorder in layered samples with nonparallel interfaces. Beyond a crossover thickness, $L > L_{co}$, the ensemble average of transmission falls more slowly than the numerical simulations for 1D and approaches an inverse rather than an exponential scaling since the impact of localization on transmission is reduced due to nonuniformity in the layers. This reflects a change in dimensionality of wave transport from 1D to 3D with increasing sample thickness or transverse disorder.

For $L < L_{co}$, measurements of intensity statistics follow 1D statistics which is associated with a segment of a log-normal distribution and even sharper drop for low

values of intensity. As the sample thickness increases, intensity statistics changes to statistics found in Q1D, in which the probability reaches its maximum at zero intensity. This is due to a topological change in the transmitted field associated with the formation of a speckle patterns with phase singularities at nulls in the intensity. The agreement of intensity statistics in the 3D slab geometry with those found in Q1D samples is a surprise since the total transmission or dimensional conductance $g$ for plane wave excitation are not clearly defined when the wave is not confined laterally. The form found for the probability density of intensity depends on a single localization parameter and applies as long the number of singularities per coherence area is the same as in generic Gaussian speckle patterns. The parameter is the "statistical conductance" $g' = 4/3[\mathrm{var}(I) - 1]$ . This parameter reduces to the dimensionless conductance $g$ in the Q1D geometry in the absence of absorption. Waves are localized when $g' < 1$. Although transmission falls more slowly than the numerical simulation for 1D beyond the crossover point, $g'$ still falls below unity up to the thickest sample at which measurements were made of $L$ = 100. This indicates that light is localized in the anisotropic layered stack studied.

# Bibliography


[1] P. W. Anderson, Philos. Mag. **52**, 505 (1985).

[2] J. W. Goodman, *Statistical optics* (John Wiley & Sons, New York (2000)).

[3] S. John, Phys. Rev. Lett. **53**, 2169 (1984).

[4] P. Sheng, *Scattering and localization of classical waves in random media*, Vol. 8 (World Scientific Press, Singapore, 1990).

[5] P. Sebbah ed., *Wave and imaging through complex media* (Kluwer Academic Publisher, Dordrecht, 2001).

[6] S. John, Phys. Rev. Lett. **58**, 2486 (1987).

[7] E. Yablonovitch, Phys. Rev. Lett. **58**, 2059 (1987).

[8] C. M. Souloulis, *Photonic crystals and light localization in the 21st century.* (Kluwer Academic Publisher, The Netherlands, 2001).

[9] J. D. Joannopoulos, R. D. Mead, and J. N. Winn, *Photonic crystal: Molding the flow of light* (Princeton Univ. Press, Princeton, 1995).

[10] W. van Haeringen D. Lenstra ed, *Analogies in optics and microelectronics*. (North Holland, 1991).

[11] E. Abrahams, P. W. Anderson, D. C. Licciardello, and T. V. Ramakrishnan, Phys. Rev. Lett. **42**, 673 (1979).

[12] P. W. Anderson, Phys. Rev. **109**, 1492 (1958).

[13] D. J. Thouless, Phys. Rev. Lett. **39**, 1167 (1977).

[14] P. A. Lee and T. V. Ramakrishnan, Rev. Mod. Phys. **57**, 287 (1985).

[15] R. A. Webb, S. Washburn, C. P. Umbach, and R. B. Laibowitz, Phys. Rev. Lett. **54**, 2696 (1985).

[16] B. L. Altshuler, P. A. Lee and R. A. Webb, *Mesoscopic phenomena in solids*, Vol. 30 (Elsevier Science & Technology Books, 1991).

[17] B. L. Altshuler and D. E. Khmelnitskii, JETP lett. **42**, 359 (1985).

[18] F. Scheffold and G. Maret, Phys. Rev. Lett. **81**, 5800 (1998).

[19] D. S. Wiersma, P. Bartolini, A. Lagendijk, and R. Righini, Nature **390**, 671 (1997).

[20] E. Akkermans, P. E. Wolf, and R. Maynard, Phys. Rev. Lett. **56**, 1471 (1986).

[21] M. v. Albada and A. Lagendijk, Phys. Rev. Lett. **55**, 2692 (1985).

[22] B. A. v. Tiggelen, D. A. Wiersma, and A. Lagendijk, Europhys. Lett. **30**, 1 (1995).

[23] R. L. Weaver and O. I. Lobkis, Phys. Rev. Lett. **84**, 4942 (2000).

[24] P. E. Wolf and G. Maret, Phys. Rev. Lett. **55**, 2696 (1985).

[25] P. W. Anderson, D. J. Thouless, E. Abrahams, and D. S. Fisher, Phys. Rev. B, **22**, 3519 (1980).

[26] M. Ya. Azbel, Solid State Communications. **45**, 527 (1983)

[27] M.J. McKenna, R.L. Stanley, and J.D. Maynard **,** Phys. Rev. Lett. **69**, 1807 (1992).

[28] M. Stoytchev and A. Z. Genack, Phys. Rev. Lett. **79**, 309 (1997).

[29] A. Z. Genack, P. Sebbah, M. Stoytchev, and B.A. van Tiggelen, Phys. Rev. Lett. **82**, 715 (1999).

[30] A. A. Chabanov, M. Stoytchev and A. Z. Genack, Nature **404**, 850 (2000).

[31] A. A. Chabanov and A.Z. Genack, Phys. Rev. Lett. **87**, 153901 (2001).

[32] A. A. Chabanov and A.Z. Genack, Phys. Rev. Lett. **87**, 233903 (2001).

[33] L. Ye, G. Cody, M. Zhou, P. Sheng and A. N. Norris, Phys. Rev. Lett. **69**, 3080 (1992).

[34] R. Dalichaouch, J. P. Armstrong, S. Schultz, P. M. Platzman and S. L. McCall, Nature **354**, 53 (1991).

[35] M. Stoytchev and A. Z. Genack, Phys. Rev. B **55**, R8617 (1997).

[36] A. R. Ioffe and A. R. Regel, Prog. Semicond. **4**, 237 (1960).

[37] A. Z. Genack, Europhys. Lett. **11**, 733 (1990)

[38] J. T. Edwards and D. J. Thouless, J. Phys. C, **5**, 807 (1972)

[39] R. Landauer, Phil. Mag., **21**, 863 (1970)

[40] M. C. W. van Rossum and T. M. Nieuwenhuizen, Rev. Mod. Phys. **71**, 313 (1999).

[41] E. Kogan and M. Kaveh, Phys. Rev. B **52**, R3813 (1995).

[42] T. M. Nieuwenhuizen and M. C. M. v. Rossum, Phys. Rev. Lett. **74**, 2674 (1995).

[43] S. Zhang, J. Park, V. Milner, A. Z. Genack, Phys. Rev. Lett. **101**, 183901 (2008).

[44] J.-P. Fouque, J. Garnier, G. Papanicolaou, and K. Sølna, *Wave propagation and time reversal in randomly layered media* (Springer, New York, 2007).

[45] N. F. Mott, Philos. Mag. **22**, 7 (1970).

[46] M.Y. Azbel and P. Soven, Phys. Rev. B **27**, 831 (1983).

[47] A. Ioffe and A. R. Regel, Prog. Semicond. **4**, 237 (1960).

[48] S. He and J. D. Maynard, Phys. Rev. Lett. **57**, 3171 (1986).

[49] P. Sebbah, B. Hu, J. Klosner, and A. Z. Genack, Phys. Rev. Lett. **96**, 183902 (2006).

[50] O. Shapira and B. Fischer, J. Opt. Soc. Am. B **22**, 2542 (2005).

[51] A. H. Matsuda and K. Ishii, Prog. Theor. Phys. Suppl. **45**, 56 (1970).

[52] A. Chomette, B. Deveaud, A. Regreny, and G. Bastard, Phys. Rev. Lett. **57**, 1464 (1986).

[53] J. E. Sipe, P. Sheng, B. S. White, and M. H. Cohen, Phys. Rev. Lett. **60**, 108 (1988).

[54] M.V. Berry and S. Klein, Eur. J. Phys. **18**, 222 (1997).

[55] V. Milner and A. Z. Genack, Phys. Rev. Lett. **94**, 073901 (2005).

[56] J. Bertolotti, S. Gottardo, D. S. Wiersma, M. Ghulinyan, and L. Pavesi, Phys. Rev. Lett. **94**, 113903 (2005).

[57] J. B. Pendry, J. Phys. C **20**, 733 (1987).

[58] A. Z. Genack, Phys. Rev. Lett. **58**, 2043 (1987).

[59] I. Freund, D. Eliyahu, Phys. Rev. A, **45**, 6133 (1992).

[60] I. Freund, N. Shvartsman, Phys. Rev. E, **51**, 3770 (1995).

[61] J. H. Li, A. A. Lisyansky, T. D. Cheung, D. Livdan, and A. Z. Genack, Europhys. Lett. **22**, 675 (1993).

[62] R. Berkovits, M. Kaveh, and S. Feng, Phys. Rev. B **40**, 737 (1989)

[63] J. H. Li and A. Z. Genack, Phys. Rev. E **49**, 4530 (1994).

[64] P. Sheng, B. White, Z.-Q. Zhang, and G. Papanicolaou, Phys. Rev. B **34**, 4757 (1986).

[65] S. A. van Lagen, P.W. Brouwer, and C.W. J. Beenakker, Phys. Rev. E **53**, R1344 (1996).

[66] P. W. Brouwer, Phys. Rev. B **57**, 10526 (1998).

[67] S. Zhang, Y. Lockerman, A. Z. Genack, ArXiv:0904.1908.v1.

[68] A. A. Abrikosov and I. A. Ryzhkin, Adv. Phys. 27, 147 (1978).

[69] A. A. Abrikosov, Solid State Commun. **37**, 997 (1981).

[70] N. Nishiguchi, S. Tamura and F. Nori, Phys. Rev. B **48**, 2515 (1993).

[71] M. V. Berry, J. Phys. A **11**, 27 (1978).

[72] M. V. Berry and M. R. Dennis, Proc. R. Soc. A **456**, 2059 (2000).

[73] Y. Lahini, A. Avidan, F. Pozzi, M. Sorel, R. Morandotti, D. N. Christodoulides, and Y. Silberberg, Phys. Rev. Lett. **100**, 013906 (2008).

[74] S. Feng, C. Kane, P. A. Lee, and A. D. Stone, Phys. Rev. Lett. **61**, 834 (1988).

[75] P. A. Mello, Phys. Rev. Lett. **60**, 1089 (1988).

[76] P. A. Mello, E. Akkermans, and B. Shapiro, Phys. Rev. Lett. **61**, 459 (1988).

[77] S. Faez, A. Strybulevych, J. H. Page, A. Lagendijk, and B. A. van Tiggelen, Phys. Rev. Lett. **103**, 155703 (2009).

[78] A. D. Mirlin, Physics Reports, **326**, 259-382 (2000).

[79] A. D. Mirlin, Y. V. Fyodorov, A. Mildernberger, and F. Evers, Phys. Rev. Lett. **97**, 046803 (2006).

[80] L. I. Deych, M. V. Erementchouk and A. A. Lisyansky, Phys. Rev. Lett. **90**, 126601 (2003)

[81] I. M. Lifshitz, S. A. Gredeskul and L. A. Pastur, *Introduction to the theory of disordered systems* (Wiley, New York, 1988).

[82] M. J. Stephen and G. Cwilich, Phys. Rev. Lett. **59**, 285 (1987).